



HAL
open science

Argon storage and diffusion in Earth's upper mantle

Rémi Delon, Sylvie Demouchy, Yves Marrocchi, Mohamed Ali M.A. Bouhifd,
Patrick Cordier, Ahmed Addad, Pete G. Burnard

► **To cite this version:**

Rémi Delon, Sylvie Demouchy, Yves Marrocchi, Mohamed Ali M.A. Bouhifd, Patrick Cordier, et al..
Argon storage and diffusion in Earth's upper mantle. *Geochimica et Cosmochimica Acta*, 2019, 253,
pp.1-18. 10.1016/j.gca.2019.03.007 . hal-02357518

HAL Id: hal-02357518

<https://hal.univ-lorraine.fr/hal-02357518>

Submitted on 12 Nov 2019

HAL is a multi-disciplinary open access archive for the deposit and dissemination of scientific research documents, whether they are published or not. The documents may come from teaching and research institutions in France or abroad, or from public or private research centers.

L'archive ouverte pluridisciplinaire **HAL**, est destinée au dépôt et à la diffusion de documents scientifiques de niveau recherche, publiés ou non, émanant des établissements d'enseignement et de recherche français ou étrangers, des laboratoires publics ou privés.

Argon storage and diffusion in Earth's upper mantle

Rémi Delon^{1,*}, Sylvie Demouchy², Yves Marrocchi¹, Mohamed Ali Bouhifd³, Patrick Cordier⁴, Ahmed Addad⁴ and Pete G. Burnard¹

¹Centre de recherches pétrographiques et géochimiques, UMR 7358, Université de Lorraine & CNRS, 15 rue Notre Dame des Pauvres, 54500 Vandoeuvre-lès-Nancy, France.

²Géosciences Montpellier, UMR 5243, Université de Montpellier & CNRS, Montpellier, France.

³Laboratoire Magmas et Volcans, UMR 6524, Université Clermont Auvergne & CNRS, Clermont-Ferrand, France.

⁴Unité Matériaux et Transformations, UMR 8207, Université de Lille & CNRS, Villeneuve d'Ascq, France

*Correspondence to: r.delon@netcourrier.com

For submission to *Geochimica and Cosmochimica Acta*

November 2018

1 *Abstract*

2 In this study, fine-grained polycrystalline olivine was doped in static conditions with argon at
3 high pressure (0.30 ± 0.01 GPa) and high temperature (1050 ± 25 °C) during 24 h in a
4 Paterson press, and was then analysed using a step-heating extraction protocol coupled with
5 noble gas spectrometry to investigate argon storage and diffusivity in Earth's upper mantle
6 rocks. Our results show that a single diffusion mechanism controlled argon diffusion in our
7 samples during the step heating experiments. The effective diffusion in olivine has a low
8 activation energy implying that diffusivity is governed by combined argon diffusion in grain
9 boundaries and lattice. Unfortunately, the grain boundaries were not fully emptied at the end
10 of the step heating experiments. Mean values of lattice diffusion parameters were obtained
11 from our results and by reprocessing literature data ($Ea = 166 \pm 44$ kJ·mol⁻¹ and $D_0 = 10^{-7.04 \pm$
12 $^{1.13}$ m²·s⁻¹) and grain boundary diffusion parameters were determined from our data ($Ea = 22$
13 ± 5 kJ·mol⁻¹ and $D_0 = 10^{-12.87 \pm 0.3}$ m²·s⁻¹). Isotopic diffusivity ratios are constant and close to
14 the values determined by Graham's law in the C- (bulk diffusion dominated by grain
15 boundary diffusion) and A-regimes (bulk diffusion controlled by grain boundary and lattice
16 diffusion in proportion to the segregation of Ar between those sites), but vary in the B-regime
17 (bulk diffusion controlled by both grain boundary and lattice diffusion in a complex manner),
18 implying a higher isotopic fractionation in this kinetic regime. Extrapolation to typical mantle
19 grain sizes implies that around 22 % of the argon in the upper mantle can be stored at grain
20 boundaries and effective diffusion is mostly in the A-regime, suggesting a low isotopic
21 fractionation and diffusivities faster than lattice diffusivities alone. The consideration of grain
22 boundaries as a potential Ar storage site can modify equilibrium during partial melting and
23 can significantly enrich a liquid during fluid percolation. The grain size dependence of Ar
24 storage and diffusivity highlights the underestimated role of grain boundaries in upper mantle,

25 especially in zones of reduced grain size (via dynamic recrystallization) possibly followed by
26 fluid percolation and/or partial melting, such as in subduction zones or below oceanic ridges.

27
28 *1. Introduction*

29 The degassing of primitive volatile isotopes at mid-oceanic ridges such as ^3He (e.g.,
30 Lupton & Craig, 1975; Farley et al., 1995; Bianchi et al., 2010) implies that primordial
31 volatiles have been stored in the mantle since Earth's core-mantle differentiation, and are still
32 degassing into the atmosphere. Furthermore, the chemical and isotopic dichotomy between
33 mid-ocean ridge basalts (MORBs) and ocean island basalts (OIBs) indicates the chemical
34 heterogeneity of the mantle despite large-scale convection: a deep reservoir that is rich in
35 primordial isotopes and volatile elements is sampled only by OIBs (e.g., Hofmann et al.,
36 1978; Hofmann & Hart, 1978; White, 1985; Zindler & Hart, 1986; Farley et al., 1992; Hart et
37 al., 1992; Hanan & Graham, 1996; Hofmann, 2003).

38 Argon (Ar), as other noble gases, is a reliable tracer of geochemical heterogeneities since
39 it is (i) both a strongly incompatible and volatile element, and (ii) not easily recycled into the
40 mantle, except perhaps via cold subduction zones (e.g., Staudacher & Allègre, 1988; Moreira
41 & Raquin, 2007; Smye et al., 2017). Argon has three stable isotopes: two primordial isotopes
42 (^{38}Ar and ^{36}Ar) and one radiogenic isotope (^{40}Ar) produced by the radioactive decay of ^{40}K
43 with a negligible part of primordial ^{40}Ar . The K-Ar system is used to constrain the degassing
44 of the Earth's mantle and the $^{40}\text{Ar}/^{36}\text{Ar}$ ratio is a reliable tracer of mantle heterogeneities
45 because after correction for atmospheric contamination (by using the $^{20}\text{Ne}/^{22}\text{Ne}$ isotopic ratio,
46 e.g., Zhang, 2014), the value of this ratio is around 40 000 in MORBs (e.g., Burnard et al.,
47 1997; Raquin et al., 2008) and less than 10 000 in OIBs (e.g., Fisher, 1983; Hiyagon et al.,
48 1992; Honda et al., 1993; Moreira et al., 1995; Valbracht et al., 1997; Sarda et al., 2000;
49 Tieloff et al., 2000, 2002; Honda & Woodhead, 2005; Hopp & Tieloff, 2005; Raquin &
50 Moreira, 2009; Mukhopadhyay, 2012). These values suggest an OIB source that is enriched in

51 primordial isotopes and less degassed compared to the MORB source. Furthermore, the
52 $^{38}\text{Ar}/^{36}\text{Ar}$ ratio can be used to trace the origins of volatiles in the mantle. The whole-mantle
53 value $^{38}\text{Ar}/^{36}\text{Ar} = 0.188$ implies a primordial signature significantly different from the solar
54 composition ($^{38}\text{Ar}/^{36}\text{Ar} = 0.1818 \pm 0.0002$; e.g., Meshik et al., 2007) and may indicate a
55 chondritic origin for primordial argon (Moreira, 2013), as is the case for xenon (Caracausi et
56 al., 2016). This primordial isotopic signature may have been inherited from the Earth's
57 building blocks and preserved in the deep mantle since its differentiation, 4.5 Ga. To explain
58 the preservation of volatiles and primordial isotopic compositions in the OIB source, several
59 geochemical models (layered or not) have proposed an isolated OIB mantle reservoir despite
60 the expected convection of the entire mantle, including: (i) the two-layer mantle model (e.g.,
61 Allègre, 1987), (ii) the basal magma ocean model (Labrosse et al., 2007), and (iii) models
62 involving a hidden reservoir as the OIB source, such as the D'' layer (Coltice et al., 2011) or
63 outer-core material (a liquid or a solid phase) that could be incorporated in mantle plumes
64 during their formation (Porcelli & Halliday, 2001; Bouhifd et al., 2013).

65 In this study, we propose an alternative to such large-scale models to explain the
66 preservation of chemical and isotopic heterogeneities in the mantle by identifying and
67 studying microscopic Ar storage sites in mantle rocks. Indeed, high-temperature partitioning
68 experiments have shown that incompatible elements are preferentially stored at grain
69 interfaces in polycrystalline olivine (Hiraga et al., 2003, 2004, 2007), as recently confirmed
70 for grain boundaries (Bachhav et al., 2015) and along mineral dislocations (Piazolo et al.,
71 2016) by atom probe tomography performed on natural samples. The storage of noble gases
72 along grain boundaries implies that the storage capacity of mantle materials depends on grain
73 size, as is the case for helium in fine-grained lithologies (Kurz et al., 2009; Recanati et al.,
74 2012). Moreover, the segregation of an element between grain boundaries and mineral lattices
75 influences its transport through the polycrystalline material depending on the diffusion regime

76 (e.g., Mortlock, 1960; Harrison, 1961; Mishin & Herzig, 1995; Chakraborty, 2008; Dohmen
77 & Milke, 2010). This influence has been studied in several studies by modelling grain
78 boundary diffusion (Lee, 1995; Dohmen & Chakraborty, 2003; Maier, 2004; Mantsi et al.,
79 2017), and by experimental quantification (e.g., Joesten, 1991; Herzig et al., 1993; Farver &
80 Yund, 1996, 1998; Mishin & Herzig, 1999; Herzig & Divinski, 2003; Van Orman et al., 2003;
81 Herzig & Mishin, 2005; Hayden & Watson, 2007; McCaig et al., 2007). However, only a few
82 ionic diffusivities are available for silicates: OH⁻ (Lasaga, 1986), O (Farver & Yund, 1991,
83 1992, 1995; Joesten, 1991; Shimojuku et al., 2009), H (Demouchy, 2010a, 2010b), Mg
84 (Farver et al., 1994), Mg-Fe (Dohmen, 2008) and Si (Farver & Yund, 2000a, b; Shimojuku et
85 al., 2009). For He and Ar, grain boundary storage and its influence on diffusion have been
86 investigated in experimentally doped polycrystalline olivine, mimicking mantle conditions
87 (Burnard et al., 2015; Delon et al., 2018). These studies have shown that a significant amount
88 of He and Ar can be stored at grain boundaries, increasing their bulk diffusivities in fine-
89 grained olivine-rich rocks at low temperature (< 900 °C) compared to lattice diffusion alone.
90 By applying these results to the upper mantle, these studies have determined that the amount
91 of He stored at grain boundaries increases with reduced grain size, reaching 22 % of the total
92 He content at a grain size of 1 mm. These results imply increased bulk diffusivities when
93 accounting for grain boundary diffusion, even at typical mantle grain sizes of 1-7 mm (e.g.,
94 Hiraga et al., 2010), reaching the maximum value of grain boundary diffusivities at smaller
95 grain sizes ($\leq 100 \mu\text{m}$). In this study, we report new data on Ar distribution and diffusion in
96 polycrystalline olivine and constrain Ar storage and mobility in Earth's upper mantle.

97

98 2. *Materials and methods*

99 We followed a two-step experimental protocol: first, olivine powder was sintered to
100 obtain dense polycrystalline olivine with clean, dry, melt-free grain boundaries; then the

101 starting materials were doped with noble gases at high pressure (HP) and high temperature
102 (HT) using uraninite and orthoclase as the He and Ar sources, respectively. The doped
103 polycrystalline olivine samples were analyzed by step heating coupled with a noble gas mass
104 spectrometer. Helium analyses of the three samples produced and analyzed (RDPC1, RDPP1,
105 and RDPP1-2) were reported in Delon et al. (2018); here we report Ar analyses of the same
106 samples. A brief description of the experimental protocol with respect to Ar is reported
107 below; for further details see Delon et al. (2018).

108

109 *2.1. Starting material*

110 Inclusion-free, gem-like, and hydrogen-poor San Carlos olivines
111 ($\text{Mg}_{0.904}\text{Fe}_{0.092}\text{Ni}_{0.0035}\text{Cr}_{0.0003}\text{SiO}_4$) were carefully selected and then crushed and sieved to
112 obtain powders of different grain sizes. Powder grain sizes were analyzed using a Helos BF
113 laser diffraction granulometer with a He-Ne red laser. Powders were introduced into a water
114 tank and agitated before being sent to the R5 (measurement range of 2.5-875 μm , focal depth
115 of 500 mm) or R2 lens (measurement range of 0.25-87.5 μm , focal depth of 50 mm) for laser
116 diffraction analysis. The same analysis was performed a second time after 60 s of sonication
117 in the water tank to avoid grain agglomeration. The resulting olivine grain size ranges were
118 0.5-100 μm (average around 14 μm) for RDPC1, and 0.3-80 μm (average around 14 μm) for
119 RDPP1.

120 Once characterized, the olivine powders were sintered: RDPP1 at 0.30 ± 0.01 GPa and
121 1225 ± 25 °C for 5 hours in a gas-medium HP-HT apparatus (Paterson press; Paterson, 1990)
122 at Geosciences Montpellier (GM, University of Montpellier, France), and RDPC1 at $1.00 \pm$
123 0.02 GPa and 1275 ± 1 °C for 72 h with a piston cylinder apparatus at the Laboratoire
124 Magmas et Volcans (LMV, Université Clermont Auvergne, Clermont-Ferrand, France). The
125 recovered polycrystalline olivine samples were then hand-polished and cut into slices, prisms,

126 or cubes as the starting materials for the doping experiments. The experimental assemblies
127 and the different sintering conditions are reported in Table 1.

128 The texture and grain size of the polycrystalline olivine samples were characterized after
129 the sintering experiment by scanning electron microscopy (SEM), electron backscatter
130 diffraction (EBSD). SEM imaging and EBSD analyses were performed at Geosciences
131 Montpellier with a CamScan X500FE CrystalProbe, and with a 15 kV accelerating voltage,
132 3.5 nA beam current and a working distance of 20 mm under low vacuum conditions (5 Pa of
133 gaseous nitrogen). Samples were embedded in a 1-inch epoxy plug and regularly polished
134 before a final chemo-mechanical polish with a colloidal silica suspension required for EBSD.
135 Then, samples were surrounded by copper-carbon conductive tape. EBSD maps were
136 acquired with a step size of 0.2 to 4 μm (for further details on the data treatment, see
137 Demouchy et al., 2011, 2014 or Thieme et al., 2018).

138

139 *2.2. Doping at high pressure*

140 The starting materials were doped at temperature (T) of 1060 ± 25 °C and 0.30 ± 0.01
141 GPa during 24 h in the presence of an Ar source (orthoclase from Madagascar, chemical
142 composition detailed in Arnaud & Kelley, 1997) using the Paterson press at Geosciences
143 Montpellier. The doping experiment was carefully developed to mimic sub-solidus mantle
144 conditions for natural, polycrystalline, and texturally equilibrated olivine at low noble gas
145 partial pressure. After doping, the polycrystalline olivines were cut into mm-sized cubes to
146 ensure no residual doping material (orthoclase) was present during the subsequent noble gas
147 analyses and that the sample size is large enough compare to grain size to average out the
148 competing mechanisms. Thus, contamination by Ar with an atmospheric ratio can only occur
149 during the doping experiment at high pressure and high temperature (i.e., high Ar fugacity),
150 then coming from the pressure medium of the HP-HT apparatus (Ar gas vessel). Indeed, mm-

151 sized cubes are poorly affected by atmospheric contamination due to their low surface to
152 volume ratio (Protin et al., 2016). The doping conditions are reproduced in Table 1 and the
153 assembly in Fig. 1. To constrain the potential grain size variations during the doping
154 experiment, we calculate the diffusion length of silicon (Si) by using the Si diffusion
155 coefficient in dry (Dohmen et al., 2002) and wet olivine (Costa & Chakraborty, 2008) at the
156 conditions of the doping experiment (24h and 1060 °C). This diffusion length is 0.20 nm in
157 dry olivine and 23 nm in wet olivine. Since the grain size variation does not exceed these
158 diffusion lengths, we can conclude that it is very minor during the doping experiment.

159 After doping, olivine microstructures were characterized by transmission electron
160 microscopy (TEM) and high-resolution TEM (HR-TEM) at Unité Matériaux et
161 Transformations (UMET, University of Lille, France). Doubly polished thin sections (30 µm
162 thick) were ion milled at 5 kV under a low beam angle of 15° to reach electron transparency.
163 The thin foils were then covered by a thin layer of carbon before characterization using a
164 Philips CM30 microscope operating at 300 kV and a FEI® Tecnai G2-20 twin microscope
165 operating at 200 kV for TEM analyses, and a FEI Titan³ Themis 300 operating at 300 kV for
166 HR-TEM analyses.

167

168 *2.3. Noble gas analyses*

169 Analyses of argon were performed using a noble gas mass spectrometer and following a
170 step heating protocol. Analytical protocol is identical to Delon et al. (2018). The samples
171 were annealed at different temperatures (400 to 1200 °C) and the extracted amount of gas was
172 analyzed to get the Ar molar quantity released at each heating step. Then, the fractional gas
173 loss (F) from the sample at each step was calculated by dividing the molar quantity by the
174 initial total amount of Ar in the sample. It yields the diffusion coefficient D as a function of

175 the square of the radius of the diffusion domain a , following the equations (e.g., Crank, 1975;
 176 Fechtig & Kalbitzer, 1966; McDougall & Harrison, 1999):

$$\frac{D}{a^2} = \frac{\pi}{36} \cdot \frac{(F_1^2 - F_2^2)}{(t_1 - t_2)} \text{ for } F < 0.10 \quad , \quad (1)$$

$$\frac{D}{a^2} = \frac{1}{(t_1 - t_2)} \cdot \left[\frac{1}{3} (F_2 - F_1) + \frac{2}{\pi} \left(\sqrt{1 - \frac{\pi}{3} F_2} - \sqrt{1 - \frac{\pi}{3} F_1} \right) \right] \text{ for } 0.10 < F < 0.85 \quad , \quad (2)$$

$$\frac{D}{a^2} = \frac{1}{\pi^2(t_2 - t_1)} \ln \left(\frac{1 - F_1}{1 - F_2} \right) \text{ for } F > 0.85 \quad , \quad (3)$$

177 where t_1 and t_2 are the respective extraction durations and F_1 and F_2 the respective cumulative
 178 fractional gas losses at the beginning and at end of each step. The diffusion coefficients D (or
 179 D/a^2 ratio when the value of a is unknown) are obtained as a function of $1/T$, and used to
 180 extract the diffusion parameters: (i) the activation energy Ea and (ii) the pre-exponential
 181 factor D_0 (or D_0/a^2 if a unknown). Noble gas analyses were achieved at Centre de Recherches
 182 Pétrographiques et Géochimiques (CRPG, Université de Lorraine, Nancy, France) using a
 183 Helix MC Plus mass spectrometer calibrated using aliquots (≈ 0.3 cc) of an in-house Ar
 184 standard with known molar quantities of ^{40}Ar , ^{38}Ar , and ^{36}Ar . The ^{40}Ar signal was collected
 185 on a faraday cup coupled with a $10^{11} \Omega$ amplifier, and the ^{38}Ar and ^{36}Ar signals were
 186 measured simultaneously on an electron multiplier CDD. For each standard run, the
 187 sensitivity of the mass spectrometer was calculated and used to measure an unknown molar
 188 quantity from an analysis. About 5 mg of doped olivine sample was placed in a container
 189 above a Nicrofer® alloy tube (inner diameter 13 mm), heated by a radiative external furnace.
 190 Blank measurements of the empty tube were performed at each temperature step for the first
 191 sample; and for others, only 5 blanks (between 0 and 1200 °C) were analyzed leading to the
 192 same results. The sample was then placed at the bottom of the tube by dropping it from the
 193 container. At each temperature step between 400 ± 1 and 1200 ± 1 °C, the temperature was
 194 increased by 25 or 50 °C and held for 15 to 30 min. Individual step sequences are reported in
 195 Table 1. The extracted gases were analyzed and background and blank corrections were

196 performed at each analysis. External error was calculated based on the sensitivities of each
197 standard, and is less than 4% per measurement, leading to a maximum external error of ± 0.02
198 on the resulting $\log(D/a^2)$ value. The samples were crushed in a vacuum and the extracted
199 gases analyzed prior to step heating analyses to investigate the amount of Ar stored in
200 intergranular porosity. The extracted Ar accounted for less than 10 % of the total Ar in the
201 samples, ensuring that no Ar stored in porosity was analyzed in the subsequent step heating
202 analyses.

203 After the final heating step, the sample was loaded in a laser chamber and melted using a
204 30 W, 10.6- μm -wavelength (CO_2) laser to extract the remaining Ar and a re-extraction was
205 performed to ensure that all Ar was extracted from the sample. This last melting step allows
206 calculation of the total amount of Ar in the sample, and thus the fractional gas loss at each
207 temperature step necessary to obtain the diffusion coefficient as a function of a^2 . Details of
208 individual step heating analyses are reported in Table 1.

209

210 3. Results

211 3.1. Microstructures

212 A SEM image of RDPC1 is available in Fig. 2a, showing clean polycrystalline olivine
213 with an equilibrated texture, and melt-free grain boundaries. Low residual porosity is the
214 result of imperfect compaction at 0.3 and 1 GPa. As Ar is a volatile element, these defects
215 could potentially store a significant amount of Ar, but the amount stored in porosity is small
216 (less than 10 % of the total Ar) as previously discussed in section 2.3. EBSD maps show that
217 grain sizes range from 1 to 50 μm (averaging 16.3 μm) for RDPC1, and from 1 to 30 μm
218 (averaging 8.8 μm) for RDPP1. These grain size ranges and average values are slightly
219 different from those obtained by laser diffraction. In the case of RDPC1, the increased grain
220 size probably resulted from olivine grain growth during piston-cylinder sintering experiments

221 since they were long duration experiments (ca. three days). For RDPP1, the decreased grain
222 size might be due to brittle/cataclastic deformation during cold pressing, as the sintering
223 experiments were too short to permit significant grain growth.

224 TEM images are shown in Fig. 2b and 2c. TEM analyses revealed the presence of
225 dislocations, rare pores at junctions, and a few nanometric bubbles that were not
226 systematically linked with dislocations or grain boundaries (e.g., Burnard et al., 2015; Delon
227 et al., 2018). Grain boundaries are linear or quasi linear, indicating a near-equilibrium texture.
228 RDPC1 shows a lower dislocation density than RDPP1, which might be due to microstructure
229 recovery during the longer annealing period at higher temperature and pressure (Farla et al.,
230 2011). HR-TEM analyses (Fig. 2d), confirmed that grain boundaries are highly crystalline and
231 melt-free. Additional SEM and TEM images are available in Delon et al. (2018).

232

233 3.2. Ar diffusivity

234 Diffusion coefficients are reported in Fig. 3. The detailed data treatment is provided in
235 supplementary material as well as the plots $T = f(t)$, $F = f(t)$, and the isotopic ratios as a
236 function of F . To constrain the fit of our data by one or two linear regressions (as it the case
237 for He data, see Delon et al., 2018), we used a F -test (see appendix for further details).
238 Despite some scatter in the data, the fit of diffusivities by one single linear regression cannot
239 be rejected and represents the simplest model. Thus, we performed only one linear regression
240 and obtained activation energies for ^{40}Ar diffusion of 37 ± 10 , 39 ± 14 , and $22 \pm 10 \text{ kJ}\cdot\text{mol}^{-1}$,
241 for RDPC1, RDPP1 and RDPP1-2, respectively. The extracted diffusion parameters are
242 reported in Table 2. Linear regression on ^{38}Ar and ^{36}Ar diffusivities shows approximately
243 the same Ea values for ^{38}Ar diffusion ($35 \pm 12 \text{ kJ}\cdot\text{mol}^{-1}$ and $20 \pm 16 \text{ kJ}\cdot\text{mol}^{-1}$ for RDPC1 and
244 RDPP1-2, respectively) and ^{36}Ar diffusion ($33 \pm 12 \text{ kJ}\cdot\text{mol}^{-1}$ and $27 \pm 12 \text{ kJ}\cdot\text{mol}^{-1}$ for RDPC1
245 and RDPP1-2, respectively; Table 2). Errors are reported at 2σ .

246 These results could be influenced by the release of Ar trapped in pores during the last
 247 laser extraction, which can modify the total amount of Ar in the sample and thus, the resulting
 248 diffusivities because of Eqs. (1-3). Indeed, reducing the total amount of Ar by 10 % enhances
 249 the resulting pre-exponential factor although the activation energy is not modified in the error
 250 bar. However, this process did not influence He data since the resulting pre-exponential
 251 factors agreed with literature data, meaning that He extracted during the fusing stage mainly
 252 comes from the crystal lattice and grain boundaries (and not from pores). Thus, the same
 253 conclusion can be done for Ar as the same storage behavior is expected.

254

255 3.3. Segregation factor

256 To investigate Ar storage in grain boundaries, the segregation factor (s) between grain
 257 boundaries and the crystal lattice is defined as the ratio between the concentrations in grain
 258 boundaries (C^{GB}) and in the crystal lattice (C^{LAT}):

$$s = \frac{C^{GB}}{C^{LAT}} \quad (4)$$

259 Similarly, the molar segregation factor (χ) is defined as the ratio between the molar quantities
 260 in grain boundaries (X^{GB}) and in the lattice (X^{LAT}):

$$\chi = \frac{X^{GB}}{X^{LAT}} \quad (5)$$

261 χ was calculated by considering X^{GB} as being the total amount of the element extracted in the
 262 temperature range where both grain boundary and lattice diffusions occur, and X^{LAT} is the total
 263 amount of the element subtracted to X^{GB} . However, only a single diffusion process with a low
 264 Ea is observed in this study, suggesting that grain boundaries retained Ar through the entire
 265 step heating experiments (up to 1100 °C). In this case, only a minimum X^{GB} value can be
 266 determined and, thus, minimum values of the segregation factor (s_{min}) and the molar
 267 segregation factor (χ_{min}). Here, we obtained χ_{min} by defining X^{GB} as the total amount of Ar

268 extracted during the step heating experiments, and X^{LAT} as the amount of Ar extracted during
 269 the last laser melting. Then, s_{min} was determined from χ_{min} since:

$$s = \frac{C^{GB}}{C^{LAT}} = \frac{X^{GB}V^{LAT}}{X^{LAT}V^{GB}} = \frac{\chi}{v} \quad , \quad (6)$$

270 where V^{LAT} and V^{GB} are the respective lattice and grain boundary volumes, and $v = 2.84 \cdot \delta/d$ is
 271 the volume fraction of grain boundaries in the sample (Hiraga & Kohlstedt, 2009) based on
 272 the grain boundary width δ (1 nm, Hayden & Watson, 2007) and grain size d (16.3 μm for
 273 RDPC1 and 8.8 μm for RDPP1 and RDPP1-2). The minimum molar segregation factors and
 274 segregation factors are reported in Table 2.

275

276 3.4. Isotopic diffusion

277 Since Ar isotopes could be analyzed, isotopic diffusion has been determined by
 278 comparing the diffusion coefficients of the different Ar isotopes. Graham's law predicts that,
 279 in gases, the mobility ratio of different isotopes is equal to the square root of the inverse of
 280 their mass (m) ratio. This law can be applied to the diffusion coefficient ratio as:

$$\frac{D_x}{D_y} = \left(\frac{m_y}{m_x} \right)^\beta \quad , \quad (7)$$

281 where x and y are two different isotopes of the same element and $\beta=0.5$ in gases. A similar
 282 law is generally assumed for noble gas isotopes in solids (Burnard & Harrison, 2005; Craig &
 283 Lupton, 1976; Kaneoka, 1980; Pinti et al., 1999; Ruzié & Moreira, 2010; Yamamoto et al.,
 284 2009), except in glasses below their glass transition temperature (see Amalberti et al., 2016).
 285 We calculated D_{40}/D_{36} , D_{40}/D_{38} , and D_{36}/D_{38} (subscripts denote the Ar isotopic mass number)
 286 for each temperature step for samples RDPC1 and RDPP1-2 and compared them to Graham's
 287 law. Results are reported in Fig. 4 and the ratios are relatively constant at low temperatures (T
 288 ≤ 800 °C) but vary widely at higher temperatures (900-1200 °C). The low-temperature
 289 averages of these ratios ($D_{40}/D_{36} = 0.89 \pm 0.06$, $D_{40}/D_{38} = 0.83 \pm 0.12$, and $D_{36}/D_{38} = 0.90 \pm$

290 0.10, calculated excluding data beyond the 2σ range, i.e., one point for each ratio) are close to
291 the values predicted by Graham's law (0.95, 0.97 and 1.08 respectively). These isotopic
292 diffusion coefficient ratios are slightly inferior to 1 and could be below the values predicted
293 by Graham's law (except for the D_{36}/D_{38} ratio), suggesting that diffusive isotopic
294 fractionation could be slightly more important than estimated by Graham's law. Whereas at
295 higher temperatures, the ratios are more variable and farther from those predicted by
296 Graham's law, indicating a more important isotopic fractionation.

297

298 4. Discussion

299 4.1. Ar source during the doping experiments

300 Although the Ar source used in the doping experiments was orthoclase containing quasi-
301 exclusively the ^{40}Ar isotope, ^{38}Ar and ^{36}Ar signals were above blank intensities for RDPC1
302 and RDPP1-2, suggesting that Ar was also incorporated from the pressure medium (Ar gas) in
303 the HP-HT apparatus. Moreover, the $^{40}\text{Ar}/^{36}\text{Ar}$ isotopic ratios of the samples were 352 ± 28
304 and 292 ± 23 for RDPC1 and RDPP1-2, respectively, very close to the atmospheric ratio
305 (298.56 ± 0.31 , Lee et al., 2006) and that of the pressure medium in the Paterson press. These
306 results indicate that most of the Ar in the samples was incorporated from the pressure medium
307 during the long-duration doping experiments. Thus, Ar was incorporated at high fugacity, and
308 the doping conditions did not directly mimic mantle conditions. Nevertheless, as diffusion
309 occurs during the step heating analyses, Ar incorporation at high pressure does not affect the
310 accuracy of the resulting diffusivities, except maybe in modifying the initial concentration
311 profile in the polycrystalline sample (whereas Eqs. 1-3 were developed for a homogeneous
312 concentration; Crank, 1975; Fechtig & Kalbitzer, 1966; McDougall & Harrison, 1999).
313 However, as demonstrated in the recent study by Delon et al. (2018), the calculated diffusion
314 parameters were not affected by the initial concentration profile, implying that the

315 diffusivities obtained here are accurate and representative of Ar diffusivities in fine-grained
316 polycrystalline olivine. Only the segregation of Ar between grain boundaries and the crystal
317 lattice cannot be considered as representative of mantle rocks.

318

319 *4.2. Interpretation of the diffusion parameters*

320 In previous studies, a change of slope was observed at the transition temperature for He
321 and Ar diffusivities, which was interpreted as two different diffusion processes occurring as a
322 function of temperature (see Burnard et al., 2015; Delon et al., 2018): (i) lattice diffusion
323 occurs above the transition temperature, and (ii) combined lattice and grain boundary
324 diffusion occur below the transition temperature. Delon et al. (2018) referred to lattice
325 diffusion as LAT, grain boundary diffusion as GB, and diffusion controlled by both lattice
326 and grain boundary diffusion as LAT+GB, and we follow that usage here. However, in our
327 current study, the F-test do not reject the model with only one linear regression to fit our data,
328 thus only a single linear regression was performed for each sample. The calculated diffusion
329 parameters show that the three analyzed samples were governed by the same diffusion
330 process with a low Ea . These low Ea values indicate that most of the Ar extracted during step
331 heating experiments was released from a poorly retentive storage site. It is therefore important
332 to refer to previous studies to identify the diffusion mechanisms controlling Ar mobility in our
333 polycrystalline samples.

334 The Ea values obtained in this study are in agreement with those calculated for the
335 LAT+GB temperature range in Burnard et al. (2015), at least for one of their samples,
336 suggesting that only LAT+GB temperature range is observed here. The other sample from
337 Burnard et al. (2015) shows an Ea value of $114 \text{ kJ}\cdot\text{mol}^{-1}$, but this value was mostly controlled
338 by one diffusion coefficient obtained at $450 \text{ }^\circ\text{C}$. Indeed, an r^2 value of 0.10 instead of 0.68 is
339 obtained if this point is excluded from the regression. For this reason, the diffusion parameters

340 of the LAT+GB temperature range for this sample will not be compared to our data.
341 Moreover, the Ea values from this study are also consistent with reported values for He
342 diffusivities in the LAT+GB temperature range (Burnard et al., 2015; Delon et al., 2018).

343 We interpret the absence of the transition between the LAT and the LAT+GB processes to
344 indicate that the step heating experiments were not long enough or did not reach sufficiently
345 high temperatures. Indeed, the transition temperature is reached only when grain boundaries
346 are fully emptied (Delon et al., 2018), meaning that Ar was not fully extracted from grain
347 boundaries during the step heating experiments in this study. Thus, only the LAT+GB
348 temperature range is identified here.

349

350 *4.3. Lattice diffusion*

351 Because we were only able to observe LAT+GB, Ar diffusion parameters in the olivine
352 crystal lattice alone cannot be directly determined. However, literature data can be used to
353 estimate these parameters. Only a few studies have focused on Ar diffusion in the olivine
354 lattice: Futagami et al. (1993) reported $Ea = 135 \pm 12 \text{ kJ}\cdot\text{mol}^{-1}$ and $\log(D_0) = -7.84 \pm 0.62$ for
355 Ar diffusion in synthetic ion-implanted forsterite, and Thomas et al. (2008) reported $Ea = 42$
356 $\pm 2 \text{ kJ}\cdot\text{mol}^{-1}$ and $\log(D_0) = -19.14 \pm 0.1$ (D_0 in $\text{m}^2\cdot\text{s}^{-1}$) for Ar diffusion in previously polished
357 iron-free forsterite experimentally doped at high Ar pressure. The low diffusivities reported
358 by Thomas et al. (2008) would indicate that Ar behaves compatibly in mantle rocks (Watson
359 et al., 2007), but their values can also be explained by a high population of nanometric defects
360 at the sample surface (possibly due to polishing before the doping experiments or to analytical
361 limitations) and by Ar incorporation at high fugacity. For these reasons, we avoid further
362 discussion of their diffusion parameters. Ar diffusion has also been investigated in
363 experimentally doped polycrystalline olivine (Burnard et al., 2015). They obtained diffusion
364 parameters for HT lattice diffusion in two samples: $Ea = 338 \pm 98 \text{ kJ}\cdot\text{mol}^{-1}$, $\log(D_0) = 0.32 \pm$

365 4.49 above 950 °C and $Ea = 445 \pm 90 \text{ kJ}\cdot\text{mol}^{-1}$, $\log(D_0) = 2.47 \pm 2.11$ with D_0 in $\text{m}^2\cdot\text{s}^{-1}$ above
366 1100 °C. The values of the pre-exponential factors were calculated by taking $a = 150 \text{ }\mu\text{m}$
367 (half the sample size) as was suggested in Burnard et al. (2015) and confirmed by Delon et al.
368 (2018). All these diffusion parameters are presented in Fig. 5, showing that the diffusion
369 parameters reported by Burnard et al. (2015) are exceptionally high. The corresponding linear
370 regressions were highly controlled by the two highest temperature points with very fast
371 diffusivities. These high diffusivities are distinct from the trend described by the lower
372 temperature diffusivities, and by excluding them, lower diffusion parameters are obtained: Ea
373 $= 198 \pm 44 \text{ kJ}\cdot\text{mol}^{-1}$ and $\log(D_0) = -3.53 \pm 1.76$ above 950 °C and $Ea = 197 \pm 82 \text{ kJ}\cdot\text{mol}^{-1}$ and
374 $\log(D_0) = -6.24 \pm 2.86$ above 1100 °C. These recalculated diffusion parameters are in
375 agreement with those of Futagami et al. (1993), providing the mean values: $Ea = 166 \pm 44$
376 $\text{kJ}\cdot\text{mol}^{-1}$ and $D_0 = 10^{-7.04 \pm 1.13} \text{ m}^2\cdot\text{s}^{-1}$. These new diffusion parameters were obtained by
377 excluding the sample from Burnard et al. (2015) that induced an abnormally high pre-
378 exponential factor ($\log(D_0) = -3.53 \pm 1.76$).

379 The increased HT diffusivities for samples from Burnard et al. (2015) are significantly
380 faster than diffusivities extrapolated from lower temperatures and might be explained by two
381 hypotheses: (i) a change of slope related to a change in diffusion mechanism in the olivine
382 crystal lattice, or (ii) early partial melting (EPM) inducing an important partition of Ar
383 leading to its faster release. Hypothesis (i) would indicate two transition temperatures ($1075 \pm$
384 25 and $1300 \pm 100 \text{ }^\circ\text{C}$), suggesting a change in diffusion mechanism related to two different
385 Ar storage sites in the olivine lattice (e.g., different point defects), as is the case for He (Delon
386 et al., 2018). Thus, the higher transition temperature would represent the emptying of Ar from
387 a less-retentive storage site in the olivine lattice (with the lowest diffusion parameters); at
388 higher temperatures, Ar diffusion would occur only from the more-retentive storage site (with
389 higher values of the diffusion parameters). However, diffusion parameters cannot be

390 determined for this potential more-retentive storage site using the values from Burnard et al.
391 (2015) since only two temperature steps for each sample can be used to extract the
392 diffusivities of this diffusion mechanism. Hypothesis (ii) would suggest that inter- and/or
393 intra-granular EPM of olivine occurred, inducing a fast Ar release and increasing the observed
394 diffusivities at high temperature during the last heating steps. Such a phenomenon has been
395 observed in step heating experiments for Ar in pyroxenes (Cassata et al., 2011). EPM of
396 olivine has been observed between 1100 and 1500 °C (Jaoul et al., 1987), which includes the
397 transition temperature determined in Burnard et al. (2015). However, if EPM had occurred,
398 increased He diffusivities related to a He release should also be observed in the same
399 temperature range, which is not the case (Burnard et al., 2015). Therefore, we argue in favor
400 of hypothesis (i) that the observed change of Ea seems to be related to a change in the
401 diffusion mechanism induced by the emptying of a less-retentive storage site in the olivine
402 lattice.

403

404 *4.4. Grain boundary diffusion*

405 To determine the diffusion parameters for Ar in olivine grain boundaries, it is important to
406 determine the diffusion regime occurring at each temperature step. Indeed, bulk (or effective)
407 diffusion results from the combined contributions of GB and LAT depending on the diffusion
408 regime. Three diffusion regimes (A-, B- and C-) have been defined based on the lattice
409 diffusion length value (e.g., Mortlock, 1960; Dohmen & Milke, 2010; Harrison, 1961; Mishin
410 & Herzig, 1995, 1999). The A-regime occurs when the lattice diffusion length $\sqrt{D^{LAT}t}$ is
411 longer than the grain size d of the polycrystalline material. In this case, bulk diffusion appears
412 to obey Fick's law and bulk diffusivities (D^{bulk}) can be expressed as a function of lattice and
413 grain boundary diffusivities as:

$$D^{bulk} = (1 - \chi)D^{LAT} + \chi D^{GB} \quad . \quad (8)$$

414 However, this equation might not be relevant for species which highly segregate into grain
 415 boundaries and then χ can be greater than 1. More recently, Eq; (8) has been generalized by
 416 considering the concept of tortuosity leading to the following equation (Zhang & Liu, 2012):

$$D^{bulk} = \frac{(1 - v)D^{LAT} + \frac{svD^{GB}}{\theta^2}}{sv + (1 - v)} \quad , \quad (9)$$

417 with θ , the tortuosity factor for grain boundaries and v the volume fraction of grain
 418 boundaries.

419 The B-regime occurs when $d > \sqrt{D^{LAT}t} > s\delta/2$; bulk diffusivities do not follow Fick's
 420 law and D^{bulk} cannot be easily expressed as a function of D^{LAT} and D^{GB} . The C-regime occurs
 421 when $\sqrt{D^{LAT}t} < s\delta/2$ and bulk diffusion obeys Fick's law since $D^{bulk} = D^{GB}$. If the concept of
 422 tortuosity is implemented, $D^{bulk} = D^{GB}/\theta^2$ with θ the tortuosity factor (Zhang & Liu, 2012),
 423 which is typically in the range of 1.5-2.0 (Farver & Yund, 2000a) in dense polycrystals. Thus,
 424 the concept of tortuosity modifies the diffusion coefficient by a very limited factor (of 4 at the
 425 maximum value of θ), which is in the diffusivity error bar of our study and this concept will
 426 not be considered further in this study. Although these kinetic regimes have been defined for
 427 the incorporation of the diffusive species into a polycrystalline material, they can also be used
 428 for degassing experiments. Thus, during an extraction step with duration t and at constant
 429 temperature, the boundary times t' and t'' between the C- and B-regimes and between the B-
 430 and A-regimes, respectively, can be defined as:

$$t' = \frac{(s\delta)^2}{4D^{LAT}} \quad , \quad (10)$$

$$t'' = 150 \cdot \frac{d^2}{D^{LAT}} \quad . \quad (11)$$

431 However, the segregation factor s cannot be estimated in our experiments since the transition
 432 temperature between LAT and LAT+GB temperature ranges was not reached. Thus, only the

433 minimal segregation factor s_{min} can be calculated, and the minimal duration t'_{min} is defined as
434 the minimal time to reach the B-regime. This implies that $t' > t'_{min}$ thus, the C-regime occur if
435 $t' > t > t'_{min}$ and when $t < t'_{min}$.

436 The durations t'_{min} and t'' were calculated at each temperature step and for each sample by
437 determining D^{LAT} from the diffusion parameters obtained in section 4.2, and s_{min} was
438 calculated from s_{min} , the ratio between the amount of Ar extracted in later heating steps to that
439 extracted during the laser extraction, with $\delta = 1$ nm (e.g., Hayden & Watson, 2007; Hiraga et
440 al., 2007). The obtained values of t'_{min} and t'' are compiled in supplementary materials, and
441 they are compared to the extraction duration t to define the kinetic regime. These results show
442 that only the C- and B-regimes occurred during the step heating experiments (d has to be less
443 than $1.19 \mu\text{m}$ to observe the t'' transition at $1200 \text{ }^\circ\text{C}$ in our experiments). As shown above,
444 grain boundary diffusivities cannot be easily extracted from bulk diffusivities in the B-regime,
445 whereas in the C-regime, $D^{bulk} = D^{GB}$. Thus, we performed a linear regression on the
446 diffusivities obtained in the C-regime to extract the grain boundary diffusion parameters.
447 These diffusion parameters are reported in Table 3 and the grain boundary diffusivities are
448 reported in Fig. 6 for $a = 0.48 \mu\text{m}$, corresponding to the grain boundary network, and $a = 150$
449 μm , corresponding to half the sample size (i.e., half the grain size of the resulting powder
450 after crushing experiment), as proposed by Burnard et al. (2015). Comparison of grain
451 boundary and lattice diffusivities shows that for $T > 800 \text{ }^\circ\text{C}$ and $a = 0.48 \mu\text{m}$, grain boundary
452 diffusivities are slower than lattice diffusivities, which is not the case for $a = 150 \mu\text{m}$.
453 Nevertheless, as the crystalline structure is expected to be more disordered in grain
454 boundaries than in the olivine lattice, statistically, grain boundary diffusion should be faster
455 than lattice diffusion in the olivine stability field (i.e., up to at least $1400 \text{ }^\circ\text{C}$, Akaogi et al.,
456 1989). Indeed, diffusivities depend on defect concentrations (Nakamura & Schmalzried,
457 1984), which are expected to be higher in grain boundaries, except for very specific grain

458 boundary geometries (e.g., kinks; see also Dillon & Harmer, 2008a, for grain boundary
459 complexion). Thus, only the diffusivities obtained using an a value of half the sample size
460 yield grain boundary diffusivities higher than lattice diffusivities in the error range. We
461 conclude that a is equal to half the sample size for Ar diffusion in grain boundaries as is the
462 case for He (Delon et al., 2018), resulting in mean values for the grain boundary diffusion
463 parameters of $Ea = 22 \pm 5 \text{ kJ}\cdot\text{mol}^{-1}$ and $\log(D_0) = -12.87 \pm 0.3$ with D_0 in $\text{m}^2\cdot\text{s}^{-1}$.

464 Moreover, the scattering of our data remains to be explained, especially at high
465 temperature. One possibility is the remobilization of Ar trapped in residual pores since
466 crushing under vacuum might not be sufficiently effective (e.g., the resulting grain size was
467 still larger than pore size after crushing). However, the energy of remobilization is very high
468 (for He, $\sim 420 \text{ kJ}\cdot\text{mol}^{-1}$, Trull & Kurz, 1993), which implies an important (high) temperature
469 dependency. Thus, the release of Ar trapped in pores should increase with increasing
470 temperature, in enhancing diffusivities which is not observed in our data set. Instead, data
471 scattering at high temperature of our data seems to coincide with the hypothetical boundary
472 between the C- and the B-regime. It suggests that the data scattering can be explained by the
473 breakdown of Arrhenius law in the B-regime rather than a significant contribution of Ar
474 trapped in pores.

475

476 *4.5. Diffusive Ar isotopic fractionation in polycrystalline olivine*

477 As bulk diffusivities depend on the diffusive kinetic regime occurring in polycrystalline
478 rocks, diffusive isotopic fractionation should also be related to the diffusion regime. Because
479 only the C- and B-regimes occurred in our experiments, only the diffusive fractionation of Ar
480 isotopes in the C- and B-regimes can be directly studied using our data. The transition
481 between the C- and B-regimes is reported in Fig. 4 and in supplementary materials. In the C-
482 regime, the ratio between the different isotopic diffusivities seems to be constant for D_{40}/D_{36} ,

483 D_{40}/D_{38} , and D_{36}/D_{38} , suggesting that Eq. (7) can be applied. However, the value of β seems
484 to be slightly different than 0.5, at least for D_{40}/D_{38} and D_{36}/D_{38} , since the value predicted by
485 Graham's law is not within error (standard deviation) for these ratios. Because bulk diffusion
486 in the C-regime corresponds to grain boundary diffusion, we conclude that the law described
487 by Eq. (7) can be applied to grain boundaries, as is the case for noble gases in solids (Burnard
488 & Harrison, 2005; Craig & Lupton, 1976; Kaneoka, 1980; Pinti et al., 1999; Ruzi  & Moreira,
489 2010; Yamamoto et al., 2009), except perhaps in glasses at low temperature (Amalberti et al.,
490 2016).

491 The diffusive fractionations in the B-regime do not seem to follow a similar law, as shown
492 by the large variations of D_{40}/D_{36} , D_{40}/D_{38} , and D_{36}/D_{38} above the transition between the C-
493 and B-regimes (Fig. 4). These large variations do not start at the exact reported transition to
494 the B-regime, though the estimated boundary duration between the C- and B-regimes is a
495 minimum and not an absolute value (see section 3.2). Thus, several heating steps that were
496 identified as belonging to the B-regime may actually belong to the C-regime, which could
497 explain the relatively constant value of the different ratios in the first few extraction steps
498 identified in the B-regime. In later steps, the ratios vary irregularly from 1.5 to 0.5, suggesting
499 an important Ar isotopic fractionation in polycrystalline olivine. These large isotopic
500 fractionations highlight that diffusive fractionation can occur in the B-regime and should not
501 be neglected.

502 In the A-regime, the bulk diffusion coefficient is defined by Eq. (8), and the ratio between
503 the bulk diffusion coefficients of isotopes x and y (f^{bulk}) can be expressed based on the lattice
504 and grain boundary isotopic diffusivity ratios ($f^{LAT} = D_x^{LAT}/D_y^{LAT}$ and $f^{GB} = D_x^{GB}/D_y^{GB}$,
505 respectively) as:

$$f^{bulk} = \frac{D_x^{bulk}}{D_y^{bulk}} = \frac{(1 - \chi)D_x^{LAT} + \chi D_x^{GB}}{(1 - \chi)D_y^{LAT} + \chi D_y^{GB}} = \frac{(1 - \chi)D_x^{LAT} + \chi D_x^{GB}}{(1 - \chi) \frac{D_x^{LAT}}{f^{LAT}} + \chi \frac{D_x^{GB}}{f^{GB}}} \quad (12)$$

506 Thus, if $f^{LAT}=f^{GB}$, which is highly probable since these two ratios follow a similar law and are
507 close to the value given by Graham's law, then, $f^{bulk}=f^{LAT}=f^{GB}$ in the A-regime. A similar result
508 is obtained by using Eq. (9) instead of Eq. (8). Thus, Eq. (12) predicts that isotopic
509 fractionations follow a law similar to Eq. (7) in the A-regime, as is the case in the C-regime.

510

511 *4.6. Mantle implications*

512 *4.6.1. Storage of Ar in the Earth's upper mantle*

513 Since our experiments were performed on olivine, our results can only be extrapolated to
514 the Earth's upper mantle (i.e., within the olivine stability field), and differences in mineralogy
515 (i.e., monomineralic versus polymineralic) must be considered. To study the storage of Ar in
516 the upper mantle, it is important to determine the segregation factor s between the grain
517 boundaries and the olivine lattice. However, s was highly variable between our different
518 samples, and it is shown that these samples were not at the equilibrium for He (Delon et al.,
519 2018): as Ar diffusion is slower than He diffusion, Ar cannot have been at equilibrium in
520 these samples, and our segregation factors cannot be directly extrapolated to the upper mantle.
521 Nevertheless, s was always greater than 1 in our samples, highlighting that grain boundaries
522 are a potentially important Ar storage site in polycrystalline minerals.

523 Only one study has attempted to determine the s for Ar in mantle minerals (Baxter et al.,
524 2007). They found that s was bracketed between 1.47×10^5 and 4.17×10^4 in polycrystalline
525 diopside. Another method to estimate s is to determine the Ar partition coefficient between
526 olivine and silicate melt ($K^{ol-melt}$). Indeed, to the first order, the segregation between olivine
527 lattice and intergranular silicate melt is expected to be comparable to the segregation between
528 olivine lattice and grain boundaries, and thus the $K^{ol-melt}$ values are similar to the inverse of s
529 (e.g., Hiraga & Kohlstedt, 2007). Nevertheless, $K^{ol-melt}$ values for noble gases are poorly
530 constrained and vary over several orders of magnitude (e.g., Broadhurst et al., 1990, 1992;

531 Brooker et al., 1998, 2003; Chamorro et al., 2002; Heber et al., 2007; Hiyagon & Ozima,
532 1986; Jackson et al., 2013; Watson et al., 2007). Since literature data were obtained from
533 samples whose surfaces were polished before analyses, atmospheric contamination might
534 have artificially increased the reported $K^{ol-melt}$ values (as Ar is the most abundant noble gas in
535 the atmosphere, and thus the most affected by atmospheric contamination; for further details,
536 see Burnard et al., 2015; Delon et al., 2018). Thus, the true $K^{ol-melt}$ values must be lower than
537 the lowest reported values (for Ar in the upper mantle, $K^{ol-melt} < 10^{-3}$; Heber et al., 2007).
538 However, values in the 10^{-5} range have been reported for all other noble gases (e.g., Heber et
539 al., 2007; Jackson et al., 2013), suggesting that $K^{ol-melt}$ values are overestimated in the
540 literature and must also be in the 10^{-5} range, in agreement with the $1/s$ value found by Baxter
541 et al. (2007). The same estimation can be made for pyroxenes (Baxter et al., 2007; Heber et
542 al., 2007; Jackson et al., 2013).

543 We calculated the proportion of Ar in grain boundaries (X^{GB}) and in the mineral lattice
544 (X^{LAT}) as a function of grain size by using Eq. (6) and the results are presented in Fig. 7 for
545 two extreme values of s : 10^4 and 10^5 . Most Ar is stored in the lattice at typical mantle grain
546 sizes: for $s = 10^5$ (close to the value reported by Baxter et al., 2007), $X^{GB} \sim 4\%$ for $d = 7$ mm,
547 and $\sim 22\%$ for $d = 1$ mm. Thus, even at large mantle grain sizes, the amount of Ar stored in
548 grain boundaries cannot be neglected and should be considered in geochemical models. This
549 amount drastically increases for smaller grain sizes and most Ar is stored in grain boundaries
550 at $d < 285 \mu\text{m}$ for $s = 10^5$ and $d < 28 \mu\text{m}$ for $s = 10^4$. Thus, processes that result in decreased
551 grain size (i.e., upper mantle deformation) should redistribute Ar from crystal lattices to grain
552 boundaries increasing the amount of Ar that can be mobilized during fluid percolation. In
553 geological contexts where mantle deformation and fluid percolation occur together, such as
554 below mid-ocean ridges or in subduction zones, the redistribution of Ar to grain boundaries
555 can significantly change the equilibrium kinetics during partial melting and enrich the melt

556 during percolation. Though several studies have used the degassing of noble gases at oceanic
557 ridges to estimate the concentration of noble gases in the MORB source (e.g., Honda &
558 Patterson, 1999; Marty & Tolstikhin, 1998), they did not account for increased equilibrium
559 kinetics and melt enrichment during percolation, and likely overestimated the deep-Earth
560 argon concentration.

561

562 4.6.2. *Transport of Ar in the Earth's mantle*

563 To determine the diffusivity of Ar in the upper mantle, it is important to know which
564 kinetic regime occurs in mantle rocks. Thus, we calculated the boundary times t' and t''
565 defined by Eqs. (9) and (10) at mantle conditions as a function of grain size and temperature.
566 These times were determined for $\delta = 1$ nm (Hayden & Watson, 2007), and for $s = 10^5$ or 10^4
567 (the two extreme values used in section 4.6.1). The results are presented in Fig. 8 for $T = 600$,
568 800, 1000, and 1400 °C. The grain size range corresponding to special ultrafine-grained
569 material ($d < s\delta/2$) is reported following the description given by Mishin & Herzig (1995): in
570 this case, the segregation between the lattice and grain boundaries is very high, implying that
571 bulk diffusion is controlled by grain boundary diffusion ($D^{bulk} = D^{GB}$).

572 For larger grain sizes, the boundary time between the C- and B-regimes (t') does not
573 depend on grain size and occurs very rapidly for the two values of s , even at low temperature
574 (after only 7 and 0.74 years for $s = 10^5$ and 10^4 , respectively, at 600 °C). Thus, we conclude
575 that the C-regime is negligible over geological time scales in the upper mantle. The boundary
576 time between the B- and A- regimes (t'') decreases as grain size decreases and temperature
577 increases. For typical mantle grain sizes of 1 to 7 mm (Hiraga et al., 2010), the B-regime
578 ends after 21.8 Myr at 600 °C, for $d = 7$ mm, regardless of the s value, indicating that the B-
579 regime dominates for kinetic diffusion in coarse-grained mantle rocks at low temperature.
580 However, at 800 °C (a more realistic temperature value for the uppermost mantle) and for a

581 large grain size of 7 mm, the A-regime occurs after only 307 kyr, which may be neglected
582 over geological time scales. This shows that the A-regime is the main kinetic regime
583 controlling Ar diffusion in upper mantle rocks, except maybe at very low temperatures (<800
584 °C) and for large grain sizes (7 mm), which should represent only a very small portion of the
585 upper mantle (e.g., lithospheric mantle section only).

586 As the A-regime should control bulk diffusion in the upper mantle, we predict that
587 diffusive isotopic fractionation is low and follows a law similar to Eq. (7) as it is suggested by
588 Eq. (12). Bulk diffusivities are described by Eq. (8) and are controlled by both lattice and
589 grain boundary diffusivities. Thus, bulk diffusivities are highly dependent on grain size and
590 will increase for finer grain sizes (Delon et al., 2018). Since the Ar storage capacity also
591 increases with the volume fraction of grain boundaries (and thus with finer grain sizes), we
592 can identify preferential zones of Ar storage in the upper mantle where Ar transport is more
593 efficient than in the majority of the upper mantle. These zones correspond to mantle rocks
594 with a relatively small grain size induced by deformation (e.g., dynamic recrystallization),
595 such as mylonites and ultramylonites. Previous studies have reported that He concentrations
596 in bulk mylonites depend on grain size (Kurz et al., 2009; Recanati et al., 2012), and the same
597 process should be expected for Ar. To confirm this hypothesis, we must consider the presence
598 of other minerals, as pyroxenes are more Ar-retentive than olivines (higher E_a , e.g., Cassata
599 et al., 2011). Nevertheless, Ar is expected to partition between grain boundaries and the
600 pyroxene lattice, which confirms fine-grained rocks as preferential Ar storage zones in the
601 upper mantle.

602 Another important parameter to consider is pressure, as it can affect both diffusion and
603 grain boundary complexation (Hirel et al., 2017). Only one experimental study has investigated
604 the pressure effect on noble gas diffusivities in olivine between 1 atm and 2.7 GPa (Cherniak
605 & Watson, 2012). These results are in agreement with hydrogen diffusion in olivine

606 (Demouchy et al., 2016). They did not observe a pressure effect in this pressure range, though
607 models predict decreasing diffusivities with increasing pressure (e.g., Wang et al., 2015),
608 which could affect the boundary times between the different kinetic regimes by increasing t'
609 and t'' . However, as t' and t'' are mostly controlled by temperature, the pressure effect should
610 be very limited in the lithospheric mantle and the A-regime should always occur with depth
611 increase. Regarding grain boundary complexions (e.g., Dillon & Harmer, 2008b), segregation
612 between grain boundaries and the mineral lattice is pressure dependent (e.g., Hirel et al.,
613 2018; Marquardt & Faul, 2018) since the grain boundary structure becomes less disordered,
614 and denser with increasing confining pressure. Thus, grain boundary segregation should
615 decrease with increasing pressure.

616

617 5. Conclusions

618 Argon diffusivities were obtained by analyzing fractional Ar gas losses by mass
619 spectrometry on three samples, which allows constraint of Ar storage sites and mobility in
620 polycrystalline olivine.

621 • The activation energies of Ar diffusion do not vary, indicating that diffusion is
622 controlled combined lattice and grain boundary diffusions. Thus, transition temperature was
623 not reached in this study and the grain boundaries were not fully emptied at the end of the step
624 heating experiments.

625 • Since the transition temperature was not reached in our experiments, only a minimal
626 value for the segregation factor can be determined for our samples. This minimal value
627 permits calculation of the minimal time t'_{min} , necessary to reach the B-regime, and the
628 extraction steps, which were in the C-regime, can be estimated. We conclude that the C-
629 regime occurred during extraction steps below 750, 775 and 700 °C, for RDPC1, RDPP1, and
630 RDPP1-2, respectively.

631 • By reprocessing literature data, we determined the mean values of the diffusion
632 parameters for Ar diffusion in the olivine lattice to be $Ea = 166 \pm 44 \text{ kJ}\cdot\text{mol}^{-1}$ and for $D_0 = 10^{7.04 \pm 1.13} \text{ m}^2\cdot\text{s}^{-1}$. The extraction steps, which express the C-regime, were identified and a linear
633 regression on the corresponding diffusivities was performed revealing the mean grain
634 boundary Ar diffusion parameters to be $Ea = 22 \pm 5 \text{ kJ}\cdot\text{mol}^{-1}$ and $D_0 = 10^{-12.87 \pm 0.3} \text{ m}^2\cdot\text{s}^{-1}$.

636 • Ar isotopic fractionation is constant at low temperature but increases with increasing
637 temperature above 750 °C. This is interpreted as a result of the diffusion regime occurring
638 during the extraction steps. In the C-regime, the isotopic diffusion coefficient ratios seem to
639 be constant with a single value close to that predicted by Graham's law, whereas in the B-
640 regime, those ratios are variable and clearly different from 1 and the value predicted by
641 Graham's law. We obtained the same results for the A-regime by extrapolation from the C-
642 regime. Thus, isotopic fractionations are small in the A- and C-regimes, but significantly
643 larger in the B-regime.

644 • In the Earth's upper mantle, the Ar segregation factor between grain boundaries and
645 the olivine lattice can be estimated as the inverse of the Ar partition coefficient between
646 olivine and silicate melt. This value should be bracketed between 10^5 and 10^4 , in agreement
647 with previous studies. For a segregation factor of 10^5 and a grain size of 1 mm, around 22 %
648 of Ar is stored at grain boundaries. Ar storage increases with decreasing grain size, and for
649 grain sizes lower than 285 μm , the majority of Ar is stored at grain boundaries.

650 • We calculated the boundary time between the B- and A-regimes as a function of grain
651 size for the upper mantle, and showed that Ar diffusion is mostly controlled by the A-regime,
652 regardless of the segregation factor. This implies low diffusive isotopic fractionations that
653 follow a law similar to Graham's law. Moreover, bulk diffusivities in the upper mantle are
654 described by Eq. (8) and are controlled by both lattice and grain boundary diffusivities. Bulk
655 diffusivities increase with decreasing grain size as determined by previous studies.

656 • Since the storage and mobility of Ar are highly dependent on grain size, we
657 determined that preferential Ar storage zones in the upper mantle would be linked to grain
658 size reduction (e.g., by dynamic recrystallization), such as in shearing zones and associated
659 ultramylonites. Moreover, as a significant Ar storage site, grain boundaries modify the
660 equilibrium kinetics during partial melting, and increase the noble gas enrichment of the melt
661 during partial melting and fluid percolation. Thus, grain boundaries are important storage sites
662 in mantle zones where deformation is coupled with melting and fluid percolation, such as
663 below oceanic ridges or in subduction zones.

664

665 *Acknowledgments*

666 This paper is dedicated to the memory of Pete Burnard (1965-2015) who was the
667 pioneer of this project and a priceless colleague. The authors thank L. Zimmermann for his
668 help on noble gases analyses. We are also grateful to D. Laporte for his contribution to piston
669 cylinder experiments, to N. Arnaud for the use of the noble gas lab in Montpellier, and C.
670 Nevado and D. Delmas for providing high-quality thin sections for SEM and TEM analyses.
671 The TEM and EBSD-SEM national facility in Lille and Montpellier, respectively, are
672 supported by the Institut National de Sciences de l'Univers (INSU) du Centre National de la
673 Recherche Scientifique (CNRS, France). The EBSD-SEM facility in Montpellier and TEM
674 facility in Lille are also supported by the Conseil Régional Occitanie and by the Conseil
675 Régional Hauts-de-France (France), respectively. This study was mainly financed by
676 l'Agence Nationale de la Recherche through grant ANR INDIGO (ANR-14-CE33-0011).
677 This is CRPG contribution n° 2619.

678

679 *Appendix A: The F-test*

680 To constrain the modelling of our data by one or two linear regressions, we used a *F*-test

681 (e.g., Box, 1953; Chow, 1960; Hahs-Vaughn & Lomax, 2013), which consists in comparing
682 two models: a model 1 with p_1 parameters and a model 2 with p_2 parameters with $p_2 > p_1$. Here,
683 the model 1 has one linear regression ($p_1 = 2$, the slope and the intercept of the linear
684 regression) and the model 2 has two linear regressions ($p_2 = 4$, the slopes and the intercepts of
685 the two linear regressions). The F -test can be used to establish if the model 1 have to be
686 rejected or not. It consists in calculating the F value of our comparison, which is defined by
687 the following equation:

688

$$F = \frac{\left(\frac{RSS1 - RSS2}{p_2 - p_1}\right)}{\left(\frac{RSS2}{n - p_2}\right)}, \quad (A.1)$$

689 where RSS_i is the residual sum of squares of model i , and n is the number of data points. Then
690 this F -value is compared with a critical value (F_{crit}) of the F -distribution with $(p_2 - p_1, n - p_2)$
691 degrees of freedom (here $(2, n - 4)$ degrees of freedom) for some desired false-rejection
692 probability (here 0.05). The F_{crit} values are available in F tables. If the F value calculated
693 from our data is greater than F_{crit} , then the model 1 is rejected, otherwise, there is no reason to
694 reject the model 1. It does not mean that if $F < F_{crit}$, the model 2 is rejected, in this case, we
695 chose the simpler model, which is the model 1 (with fewest parameters).

696 We verified this method on the He data (see Delon et al., 2018), and especially, on the
697 sample RDPP1 where the transition between the LAT and LAT+GB domains is the most
698 blurred. In this case, $n = 21$ and $F_{crit} = 3.59$ with $(2, 17)$ degrees of freedom and with a
699 confidence level of 5 %. The resulting F value is 5.40, thus $F > F_{crit}$, which means that the
700 model with one linear regression is rejected and only the model with two linear regressions is
701 possible (i.e., one regression for the LAT + GB domain and another one for the LAT domain).

702 The F -test was performed on our Ar diffusivity data (Fig. 3), between a model 1 with one
703 linear regression and all other models with two linear regressions (only regressions with less

704 than 5 points are not tested since they are considered as not relevant). The F values for the
 705 different tests are compiled in the following table:

706

Sample	F_{crit} with a level confidence of 5 %	Number of points in the low-temperature domain	Number of points in the low-temperature domain	F value		
RDPC1	3.98	5	10	2.15		
		6	9	1.93		
		7	8	2.07		
		8	7	1.52		
		9	6	1.50		
		10	5	1.35		
RDPP1	3.63	5	15	0.77		
		6	14	1.39		
		7	13	1.23		
		8	12	1.46		
		9	11	3.50		
		10	10	1.93		
		11	9	1.97		
		12	8	1.71		
		13	7	2.18		
		14	6	1.16		
		15	5	1.11		
		RDPP1-2	3.44	5	21	3.36
				6	20	0.29
				7	19	0.47
				8	18	0.28
9	17			0.27		
10	16			0.20		
11	15			0.19		
12	14			0.32		
13	13			0.48		
14	12			0.68		
15	11			0.36		
16	10			0.36		
17	9			0.38		
18	8			0.41		
19	7			0.36		
20	6			0.40		
21	5			0.34		

707 Table A.1: Calculated F -values for each comparison between the model 1 (with a single linear
 708 regression) and models 2 (with two linear regressions, one at low temperature and another at
 709 high temperature).

710

711 Here for Ar diffusivity data, we can conclude that F is always inferior to F_{crit} and thus, the
712 model with only one linear regression is essentially never rejected and since it is the simplest
713 model with the fewest parameters, we chose this model to fit our data.

714

715 *Appendix B: Supplementary materials*

716 Supplementary data associated with this article can be found, in the online version, at ...
717 (insert DOI).

718

719 *References*

720 Akaogi, M., Ito, E., & Navrotsky, A. (1989). Olivine-modified spinel-spinel transitions in the
721 system Mg_2SiO_4 - Fe_2SiO_4 : Calorimetric measurements, thermochemical calculation,
722 and geophysical application. *Journal of Geophysical Research: Solid Earth*, *94*(B11),
723 15671–15685.

724 Allègre, C. J. (1987). Isotope geodynamics. *Earth and Planetary Science Letters*, *86*(2–4),
725 175–203.

726 Amalberti, J., Burnard, P., Laporte, D., Tissandier, L., & Neuville, D. R. (2016).

727 Multidiffusion mechanisms for noble gases (He, Ne, Ar) in silicate glasses and melts in
728 the transition temperature domain: Implications for glass polymerization. *Geochimica et*
729 *Cosmochimica Acta*, *172*, 107–126.

730 Arnaud, N. O., & Kelley, S. P. (1997). Argon behaviour in gem-quality orthoclase from
731 Madagascar: Experiments and some consequences for geochronology. *Geochimica et*
732 *Cosmochimica Acta*, *61*(15), 3227–3255. [https://doi.org/10.1016/S0016-7037\(97\)00152-](https://doi.org/10.1016/S0016-7037(97)00152-)

733 X

734 Bachhav, M., Dong, Y., Skemer, P., & Marquis, E. A. (2015). Atomic Scale Investigation of

735 Orthopyroxene and Olivine Grain Boundaries by Atom Probe Tomography. *Microscopy*
736 *and Microanalysis*, 21(S3), 1315–1316.

737 Baxter, E. F., Asimow, P. D., & Farley, K. a. (2007). Grain boundary partitioning of Ar and
738 He. *Geochimica et Cosmochimica Acta*, 71(2), 434–451.
739 <https://doi.org/10.1016/j.gca.2006.09.011>

740 Bianchi, D., Sarmiento, J. L., Gnanadesikan, A., Key, R. M., Schlosser, P., & Newton, R.
741 (2010). Low helium flux from the mantle inferred from simulations of oceanic helium
742 isotope data. *Earth and Planetary Science Letters*, 297(3), 379–386.

743 Bouhifd, M. A., Jephcoat, A. P., Heber, V. S., & Kelley, S. P. (2013). Helium in Earth's early
744 core. *Nature Geoscience*, 6(11), 982.

745 Box, G. E. P. (1953). Non-normality and tests on variances. *Biometrika*, 40(3/4), 318–335.

746 Broadhurst, C. L., Drake, M. J., Hagee, B. E., & Bernatowicz, T. J. (1990). Solubility and
747 partitioning of Ar in anorthite, diopside, forsterite, spinel, and synthetic basaltic liquids.
748 *Geochimica et Cosmochimica Acta*, 54(2), 299–309.

749 Broadhurst, C. L., Drake, M. J., Hagee, B. E., & Bernatowicz, T. J. (1992). Solubility and
750 partitioning of Ne, Ar, Kr and Xe in minerals and synthetic basaltic melts. *Geochimica et*
751 *Cosmochimica Acta*, 56(2), 709–723.

752 Brooker, R. A., Du, Z., Blundy, J. D., & Kelley, S. P. (2003). The 'zero charge' partitioning
753 behaviour of noble gases during mantle melting. *Nature*, 423(6941), 738.

754 Brooker, R. A., Wartho, J. A., Carroll, M. R., Kelley, S. P., & Draper, D. S. (1998).
755 Preliminary UVLAMP determinations of argon partition coefficients for olivine and
756 clinopyroxene grown from silicate melts. *Chemical Geology*, 147(1), 185–200.

757 Burnard, P., Demouchy, S., Delon, R., Arnaud, N. O., Marrocchi, Y., Cordier, P., & Addad,
758 A. (2015). The role of grain boundaries in the storage and transport of noble gases in the
759 mantle. *Earth and Planetary Science Letters*, 430, 260–270.

760 <https://doi.org/10.1016/j.epsl.2015.08.024>

761 Burnard, P., Graham, D., & Turner, G. (1997). Vesicle-specific noble gas analyses of“
762 popping rock”: implications for primordial noble gases in Earth. *Science*, 276(5312),
763 568–571.

764 Burnard, P., & Harrison, D. (2005). Argon isotope constraints on modification of oxygen
765 isotopes in Iceland Basalts by surficial processes. *Chemical Geology*, 216(1–2), 143–
766 156.

767 Caracausi, A., Avice, G., Burnard, P. G., Füri, E., & Marty, B. (2016). Chondritic xenon in
768 the Earth’s mantle. *Nature*, 533(7601), 82–85.

769 Cassata, W. S., Renne, P. R., & Shuster, D. L. (2011). Argon diffusion in pyroxenes:
770 Implications for thermochronometry and mantle degassing. *Earth and Planetary Science*
771 *Letters*, 304(3–4), 407–416. <https://doi.org/10.1016/j.epsl.2011.02.019>

772 Chakraborty, S. (2008). Diffusion in Solid Silicates: A Tool to Track Timescales of Processes
773 Comes of Age. *Annual Review of Earth and Planetary Sciences*, 36(1), 153–190.
774 <https://doi.org/10.1146/annurev.earth.36.031207.124125>

775 Chamorro, E. M., Brooker, R. A., Wartho, J.-A., Wood, B. J., Kelley, S. P., & Blundy, J. D.
776 (2002). Ar and K partitioning between clinopyroxene and silicate melt to 8 GPa.
777 *Geochimica et Cosmochimica Acta*, 66(3), 507–519.

778 Cherniak, D. J., & Watson, E. B. (2012). Diffusion of helium in olivine at 1atm and 2.7GPa.
779 *Geochimica et Cosmochimica Acta*, 84, 269–279.
780 <https://doi.org/10.1016/j.gca.2012.01.042>

781 Chow, G. C. (1960). Tests of equality between sets of coefficients in two linear regressions.
782 *Econometrica: Journal of the Econometric Society*, 591–605.

783 Coltice, N., Moreira, M., Hernlund, J., & Labrosse, S. (2011). Crystallization of a basal
784 magma ocean recorded by helium and neon. *Earth and Planetary Science Letters*,

785 308(1), 193–199.

786 Costa, F., & Chakraborty, S. (2008). The effect of water on Si and O diffusion rates in olivine
787 and implications for transport properties and processes in the upper mantle. *Physics of*
788 *the Earth and Planetary Interiors*, 166(1–2), 11–29.

789 Craig, H., & Lupton, J. E. (1976). Primordial neon, helium, and hydrogen in oceanic basalts.
790 *Earth and Planetary Science Letters*, 31(3), 369–385.

791 Crank, J. (1975). *The Mathematics of Diffusion: 2d Ed.* Clarendon Press.

792 Delon, R., Demouchy, S., Marrocchi, Y., Bouhifd, M. A., Barou, F., Cordier, P., ... Burnard,
793 P. G. (2018). Helium incorporation and diffusion in polycrystalline olivine. *Chemical*
794 *Geology*, 488, 105–124. [https://doi.org/https://doi.org/10.1016/j.chemgeo.2018.04.013](https://doi.org/10.1016/j.chemgeo.2018.04.013)

795 Demouchy, S. (2010a). Diffusion of hydrogen in olivine grain boundaries and implications
796 for the survival of water-rich zones in the Earth's mantle. *Earth and Planetary Science*
797 *Letters*, 295(1–2), 305–313. <https://doi.org/10.1016/j.epsl.2010.04.019>

798 Demouchy, S. (2010b). Hydrogen diffusion in spinel grain boundaries and consequences for
799 chemical homogenization in hydrous peridotite. *Contributions to Mineralogy and*
800 *Petrology*, 160(6), 887–898. <https://doi.org/10.1007/s00410-010-0512-4>

801 Demouchy, S., Mainprice, D., Tommasi, A., Couvy, H., Barou, F., Frost, D. J., & Cordier, P.
802 (2011). Forsterite to wadsleyite phase transformation under shear stress and
803 consequences for the Earth's mantle transition zone. *Physics of the Earth and Planetary*
804 *Interiors*, 184(1), 91–104.

805 Demouchy, S., Mussi, A., Barou, F., Tommasi, A., & Cordier, P. (2014). Viscoplasticity of
806 polycrystalline olivine experimentally deformed at high pressure and 900 C.
807 *Tectonophysics*, 623, 123–135.

808 Demouchy, S., Thoraval, C., Bolfan-Casanova, N., & Manthilake, G. (2016). Diffusivity of
809 hydrogen in iron-bearing olivine at 3 GPa. *Physics of the Earth and Planetary Interiors*,

810 260, 1–13.

811 Dillon, S. J., & Harmer, M. P. (2008a). Demystifying the role of sintering additives with
812 “complexion.” *Journal of the European Ceramic Society*, 28(7), 1485–1493.

813 Dillon, S. J., & Harmer, M. P. (2008b). Relating grain-boundary complexion to
814 grain-boundary kinetics I: calcia-doped alumina. *Journal of the American Ceramic*
815 *Society*, 91(7), 2304–2313.

816 Dohmen, R. (2008). A new experimental thin film approach to study mobility and partitioning
817 of elements in grain boundaries: Fe-Mg exchange between olivines mediated by
818 transport through an inert grain boundary. *American Mineralogist*, 93(5–6), 863–874.
819 <https://doi.org/10.2138/am.2008.2671>

820 Dohmen, R., & Chakraborty, S. (2003). Mechanism and kinetics of element and isotopic
821 exchange mediated by a fluid phase. *American Mineralogist*, 88(8–9), 1251–1270.

822 Dohmen, R., Chakraborty, S., & Becker, H. (2002). Si and O diffusion in olivine and
823 implications for characterizing plastic flow in the mantle. *Geophysical Research Letters*,
824 29(21), 21–26.

825 Dohmen, R., & Milke, R. (2010). Diffusion in Polycrystalline Materials: Grain Boundaries,
826 Mathematical Models, and Experimental Data. *Reviews in Mineralogy and*
827 *Geochemistry*, 72(1), 921–970. <https://doi.org/10.2138/rmg.2010.72.21>

828 Farla, R. J. M., Kokkonen, H., Gerald, J. D. F., Barnhoorn, A., Faul, U. H., & Jackson, I.
829 (2011). Dislocation recovery in fine-grained polycrystalline olivine. *Physics and*
830 *Chemistry of Minerals*, 38(5), 363–377.

831 Farley, K. A., Maier-Reimer, E., Schlosser, P., & Broecker, W. S. (1995). Constraints on
832 mantle ³He fluxes and deep-sea circulation from an oceanic general circulation model.
833 *Journal of Geophysical Research: Solid Earth*, 100(B3), 3829–3839.

834 Farley, K. A., Natland, J. H., & Craig, H. (1992). Binary mixing of enriched and undegassed

835 (primitive?) mantle components (He, Sr, Nd, Pb) in Samoan lavas. *Earth and Planetary*
836 *Science Letters*, 111(1), 183–199.

837 Farver, J. R., & Yund, R. a. (1996). Volume and grain boundary diffusion of calcium in
838 natural and hot-pressed calcite aggregates. *Contributions to Mineralogy and Petrology*,
839 123(1), 77–91. <https://doi.org/10.1007/s004100050144>

840 Farver, J. R., & Yund, R. A. (1991). Measurement of oxygen grain boundary diffusion in
841 natural, fine-grained, quartz aggregates. *Geochimica et Cosmochimica Acta*, 55(6),
842 1597–1607. [https://doi.org/10.1016/0016-7037\(91\)90131-N](https://doi.org/10.1016/0016-7037(91)90131-N)

843 Farver, J. R., & Yund, R. A. (1992). Oxygen diffusion in a fine-grained quartz aggregate with
844 wetted and nonwetted microstructures. *Journal of Geophysical Research: Solid Earth*,
845 97(B10), 14017–14029.

846 Farver, J. R., & Yund, R. A. (1995). Interphase boundary diffusion of oxygen and potassium
847 in K-feldspar/quartz aggregates. *Geochimica et Cosmochimica Acta*, 59(18), 3697–3705.
848 [https://doi.org/10.1016/0016-7037\(95\)00274-4](https://doi.org/10.1016/0016-7037(95)00274-4)

849 Farver, J. R., & Yund, R. A. (1998). Oxygen grain boundary diffusion in natural and hot-
850 pressed calcite aggregates. *Earth and Planetary Science Letters*, 161(1–4), 189–200.
851 [https://doi.org/10.1016/S0012-821X\(98\)00150-2](https://doi.org/10.1016/S0012-821X(98)00150-2)

852 Farver, J. R., & Yund, R. A. (2000a). Silicon diffusion in forsterite aggregates: Implications
853 for diffusion accommodated creep. *Geophysical Research Letters*, 27(15), 2337–2340.

854 Farver, J. R., Yund, R. A., & Rubie, D. C. (1994). Magnesium grain boundary diffusion in
855 forsterite aggregates at 1000°-1300°C and 0.1 MPa to 10 GPa. *Journal of Geophysical*
856 *Research*, 99(94), 19809–19819. <https://doi.org/10.1029/94JB01250>

857 Farver, J., & Yund, R. (2000b). Silicon diffusion in a natural quartz aggregate: constraints on
858 solution-transfer diffusion creep. *Tectonophysics*, 325(3–4), 193–205.

859 Fechtig, H., & Kalbitzer, S. (1966). The diffusion of argon in potassium-bearing solids. In

860 *Potassium argon dating* (pp. 68–107). Springer.

861 Fisher, D. E. (1983). Rare gases from the undepleted mantle? *Nature*, 305(5932), 298–300.

862 Futagami, T., Ozima, M., Nagal, S., & Aoki, Y. (1993). Experiments on thermal release of
863 implanted noble gases from minerals and their implications for noble gases in lunar soil
864 grains. *Geochimica et Cosmochimica Acta*, 57(13), 3177–3194.
865 [https://doi.org/10.1016/0016-7037\(93\)90302-D](https://doi.org/10.1016/0016-7037(93)90302-D)

866 Hahs-Vaughn, D. L., & Lomax, R. G. (2013). *Statistical concepts: A second course*.
867 Routledge.

868 Hanan, B. B., & Graham, D. W. (1996). Lead and helium isotope evidence from oceanic
869 basalts for a common deep source of mantle plumes. *Science*, 272(5264), 991.

870 Harrison, L. G. (1961). Influence of dislocations on diffusion kinetics in solids with particular
871 reference to the alkali halides. *Transactions of the Faraday Society*, 57, 1191.
872 <https://doi.org/10.1039/tf9615701191>

873 Hart, S. R., Hauri, E. H., Oschmann, L. A., & Whitehead, J. A. (1992). Mantle plumes and
874 entrainment: isotopic evidence. *Science*, 256(5056), 517.

875 Hayden, L. a, & Watson, E. B. (2007). A diffusion mechanism for core-mantle interaction.
876 *Nature*, 450(7170), 709–711. <https://doi.org/10.1038/nature06380>

877 Heber, V. S., Brooker, R. A., Kelley, S. P., & Wood, B. J. (2007). Crystal–melt partitioning of
878 noble gases (helium, neon, argon, krypton, and xenon) for olivine and clinopyroxene.
879 *Geochimica et Cosmochimica Acta*, 71(4), 1041–1061.

880 Herzig, C., & Divinski, S. V. (2003). Grain Boundary Diffusion in Metals: Recent
881 Developments. *Materials Transaction*, 44(1), 14–27.
882 <https://doi.org/10.2320/matertrans.44.14>

883 Herzig, C., & Mishin, Y. (2005). Grain boundary diffusion in metals. *Diffusion in Condensed
884 Matter SE - 8*, 337–366. https://doi.org/10.1007/3-540-30970-5_8

885 Herzig, C., Geise, J. & Mishin, Y.M. (1993). Grain Boundary Diffusion and Grain Boundary
886 Segregation of Tellurium in Silver. *Acta Metallurgica et Materialia*, 41(6), 1683–1691.

887 Hiraga, T., Anderson, I. M., & Kohlstedt, D. L. (2003). Chemistry of grain boundaries in
888 mantle rocks. *American Mineralogist*, 88(7), 1015–1019.
889 <https://doi.org/10.1038/nature02259>

890 Hiraga, T., Anderson, I. M., & Kohlstedt, D. L. (2004). Grain boundaries as reservoirs of
891 incompatible elements in the Earth’s mantle. *Nature*, 427(6976), 699–703.
892 <https://doi.org/10.1038/nature02259>

893 Hiraga, T., Hirschmann, M. M., & Kohlstedt, D. L. (2007). Equilibrium interface segregation
894 in the diopside-forsterite system II: Applications of interface enrichment to mantle
895 geochemistry. *Geochimica et Cosmochimica Acta*, 71(5), 1281–1289.
896 <https://doi.org/10.1016/j.gca.2006.11.020>

897 Hiraga, T., & Kohlstedt, D. L. (2007). Equilibrium interface segregation in the diopside –
898 forsterite system I : Analytical techniques , thermodynamics , and segregation
899 characteristics, 71, 1266–1280. <https://doi.org/10.1016/j.gca.2006.11.019>

900 Hiraga, T., & Kohlstedt, D. L. (2009). Systematic distribution of incompatible elements in
901 mantle peridotite: Importance of intra- and inter-granular melt-like components.
902 *Contributions to Mineralogy and Petrology*, 158(2), 149–167.
903 <https://doi.org/10.1007/s00410-009-0375-8>

904 Hiraga, T., Tachibana, C., Ohashi, N., & Sano, S. (2010). Grain growth systematics for
905 forsterite ?? enstatite aggregates: Effect of lithology on grain size in the upper mantle.
906 *Earth and Planetary Science Letters*, 291(1–4), 10–20.
907 <https://doi.org/10.1016/j.epsl.2009.12.026>

908 Hirel, P., Bouobda Moladje, G. F., Carrez, P., & Cordier, P. (2017). Systematic Study of
909 Grain Boundaries in Periclase MgO Using Atomic-Scale Simulations. In *AGU Fall*

- 910 *Meeting Abstracts.*
- 911 Hirel, P., Moladje, G. F. B., Carrez, P., & Cordier, P. (2018). Systematic theoretical study of
912 [001] symmetric tilt grain boundaries in MgO from 0 to 120 GPa. *Physics and Chemistry*
913 *of Minerals*, 1–13.
- 914 Hiyagon, H., & Ozima, M. (1986). Partition of noble gases between olivine and basalt melt.
915 *Geochimica et Cosmochimica Acta*, 50(9), 2045–2057.
- 916 Hiyagon, H., Ozima, M., Marty, B., Zashu, S., & Sakai, H. (1992). Noble gases in submarine
917 glasses from mid-oceanic ridges and Loihi seamount: constraints on the early history of
918 the Earth. *Geochimica et Cosmochimica Acta*, 56(3), 1301–1316.
- 919 Hofmann, A. W. (2003). Sampling mantle heterogeneity through oceanic basalts: isotopes and
920 trace elements. *Treatise on Geochemistry*, 2, 568.
- 921 Hofmann, A. W., & Hart, S. R. (1978). An assessment of local and regional isotopic
922 equilibrium in the mantle. *Earth and Planetary Science Letters*, 38(1), 44–62.
- 923 Hofmann, A. W., White, W. M., & Whitford, D. J. (1978). Geochemical constraints on mantle
924 models: the case for a layered mantle, Carnegie Inst. *Washington Yearb*, 77, 548–562.
- 925 Honda, M., McDougall, I., Patterson, D. B., Doulgeris, A., & Clague, D. A. (1993). Noble
926 gases in submarine pillow basalt glasses from Loihi and Kilauea, Hawaii: a solar
927 component in the Earth. *Geochimica et Cosmochimica Acta*, 57(4), 859–874.
- 928 Honda, M., & Patterson, D. B. (1999). Systematic elemental fractionation of mantle-derived
929 helium, neon, and argon in mid-oceanic ridge glasses. *Geochimica et Cosmochimica*
930 *Acta*, 63(18), 2863–2874.
- 931 Honda, M., & Woodhead, J. D. (2005). A primordial solar-neon enriched component in the
932 source of EM-I-type ocean island basalts from the Pitcairn Seamounts, Polynesia. *Earth*
933 *and Planetary Science Letters*, 236(3), 597–612.
- 934 Hopp, J., & Trierloff, M. (2005). Refining the noble gas record of the Réunion mantle plume

935 source: Implications on mantle geochemistry. *Earth and Planetary Science Letters*,
936 240(3), 573–588.

937 Jackson, C. R. M., Parman, S. W., Kelley, S. P., & Cooper, R. F. (2013). Constraints on light
938 noble gas partitioning at the conditions of spinel-peridotite melting. *Earth and Planetary
939 Science Letters*, 384, 178–187.

940 Jaoul, O., Houlier, B., Cheraghmakani, M., Pichon, R., & Liebermann, R. C. (1987). Surface
941 destabilization and laboratory-induced non-stoichiometry in San Carlos olivine. *Physics
942 and Chemistry of Minerals*, 15(1), 41–53.

943 Joesten, R. (1991). Grain-boundary diffusion kinetics in silicate and oxide minerals. In
944 *Diffusion, atomic ordering, and mass transport* (pp. 345–395). Springer.

945 Kaneoka, I. (1980). Rare gas isotopes and mass fractionation: an indicator of gas transport
946 into or from a magma. *Earth and Planetary Science Letters*, 48(2), 284–292.

947 Karato, S. (1989). Grain growth kinetics in olivine aggregates. *Tectonophysics*, 168(4), 255–
948 273. [https://doi.org/10.1016/0040-1951\(89\)90221-7](https://doi.org/10.1016/0040-1951(89)90221-7)

949 Kurz, M. D., Warren, J. M., & Curtice, J. (2009). Mantle deformation and noble gases :
950 Helium and neon in oceanic mylonites. *Chemical Geology*, 266(1–2), 10–18.
951 <https://doi.org/10.1016/j.chemgeo.2008.12.018>

952 Labrosse, S., Hernlund, J. W., & Coltice, N. (2007). A crystallizing dense magma ocean at the
953 base of the Earth's mantle. *Nature*, 450(7171), 866.

954 Lasaga, A. C. (1986). Metamorphic reaction rate laws and development of isograds.
955 *Mineralogical Magazine*, 50(September), 359–373.
956 <https://doi.org/10.1180/minmag.1986.050.357.02>

957 Lee, J.-Y., Marti, K., Severinghaus, J. P., Kawamura, K., Yoo, H.-S., Lee, J. B., & Kim, J. S.
958 (2006). A redetermination of the isotopic abundances of atmospheric Ar. *Geochimica et
959 Cosmochimica Acta*, 70(17), 4507–4512.

960 Lee, J. K. W. (1995). Multipath diffusion in geochronology. *Contributions to Mineralogy and*
961 *Petrology*, 120(1), 60–82. <https://doi.org/10.1007/BF00311008>

962 Lupton, J. E., & Craig, H. (1975). Excess ^3He in oceanic basalts: evidence for terrestrial
963 primordial helium. *Earth and Planetary Science Letters*, 26(2), 133–139.

964 Maier, J. (2004). *Physical chemistry of ionic materials: ions and electrons in solids*. John
965 Wiley & Sons.

966 Mantsi, B., Sator, N., & Guillot, B. (2017). Structure and transport at grain boundaries in
967 polycrystalline olivine: An atomic-scale perspective. *Geochimica et Cosmochimica Acta*,
968 219, 160–176.

969 Marquardt, K., & Faul, U. H. (2018). The structure and composition of olivine grain
970 boundaries: 40 years of studies, status and current developments. *Physics and Chemistry*
971 *of Minerals*, 1–34.

972 Marty, B., & Tolstikhin, I. N. (1998). CO_2 fluxes from mid-ocean ridges, arcs and plumes.
973 *Chemical Geology*, 145(3), 233–248.

974 McCaig, A., Covey-Crump, S. J., Ismail, W. Ben, & Lloyd, G. E. (2007). Fast diffusion along
975 mobile grain boundaries in calcite. *Contributions to Mineralogy and Petrology*, 153(2),
976 159–175.

977 McDougall, I., & Harrison, T. M. (1999). *Geochronology and Thermochronology by the*
978 *$^{40}\text{Ar}/^{39}\text{Ar}$ Method*. Oxford University Press on Demand.

979 Meshik, A., Mabry, J., Hohenberg, C., Marrocchi, Y., Pravdivtseva, O., Burnett, D., ...
980 Allton, J. (2007). Constraints on neon and argon isotopic fractionation in solar wind.
981 *Science*, 318(5849), 433–435.

982 Mishin, Y., & Herzig, C. (1995). Diffusion in fine-grained materials: Theoretical aspects and
983 experimental possibilities. *Nanostructured Materials*, 6(5–8), 859–862.
984 [https://doi.org/10.1016/0965-9773\(95\)00195-6](https://doi.org/10.1016/0965-9773(95)00195-6)

- 985 Mishin, Y., & Herzig, C. (1999). Grain boundary diffusion: recent progress and future
986 research. *Materials Science and Engineering: A*, 260(1–2), 55–71.
987 [https://doi.org/10.1016/S0921-5093\(98\)00978-2](https://doi.org/10.1016/S0921-5093(98)00978-2)
- 988 Moreira, M. (2013). Noble gas constraints on the origin and evolution of Earth’s volatiles.
989 *Geochemical Perspectives*, 2(2), 229–230.
- 990 Moreira, M., & Raquin, A. (2007). The origin of rare gases on Earth: The noble gas
991 “subduction barrier” revisited. *Comptes Rendus Geoscience*, 339(14), 937–945.
- 992 Moreira, M., Staudacher, T., Sarda, P., Schilling, J.-G., & Allègre, C. J. (1995). A primitive
993 plume neon component in MORB: the Shona ridge-anomaly, South Atlantic (51–52 S).
994 *Earth and Planetary Science Letters*, 133(3–4), 367–377.
- 995 Mortlock, A. J. (1960). The effect of segregation on the solute diffusion enhancement due to
996 the presence of dislocations. *Acta Metallurgica*, 8(2), 132–134.
- 997 Mukhopadhyay, S. (2012). Early differentiation and volatile accretion recorded in deep-
998 mantle neon and xenon. *Nature*, 486(7401), 101–104.
- 999 Nakamura, A., & Schmalzried, H. (1984). On the Fe²⁺–Mg²⁺-Interdiffusion in Olivine (II).
1000 *Berichte Der Bunsengesellschaft Für Physikalische Chemie*, 88(2), 140–145.
- 1001 Paterson, M. S. (1990). Rock deformation experimentation. *The Brittle-Ductile Transition in*
1002 *Rocks*, 187–194.
- 1003 Piazzolo, S., La Fontaine, A., Trimby, P., Harley, S., Yang, L., Armstrong, R., & Cairney, J.
1004 M. (2016). Deformation-induced trace element redistribution in zircon revealed using
1005 atom probe tomography. *Nature Communications*, 7.
- 1006 Pinti, D. L., Wada, N., & Matsuda, J. (1999). Neon excess in pumice: volcanological
1007 implications. *Journal of Volcanology and Geothermal Research*, 88(4), 279–289.
- 1008 Porcelli, D., & Halliday, A. N. (2001). The core as a possible source of mantle helium. *Earth*
1009 *and Planetary Science Letters*, 192(1), 45–56.

- 1010 Protin, M., Blard, P.-H., Marrocchi, Y., & Mathon, F. (2016). Irreversible adsorption of
1011 atmospheric helium on olivine: A lobster pot analogy. *Geochimica et Cosmochimica*
1012 *Acta*, 179, 76–88.
- 1013 Raquin, A., & Moreira, M. (2009). Atmospheric $^{38}\text{Ar}/^{36}\text{Ar}$ in the mantle: implications for
1014 the nature of the terrestrial parent bodies. *Earth and Planetary Science Letters*, 287(3),
1015 551–558.
- 1016 Raquin, A., Moreira, M. A., & Guillon, F. (2008). He, Ne and Ar systematics in single
1017 vesicles: mantle isotopic ratios and origin of the air component in basaltic glasses. *Earth*
1018 *and Planetary Science Letters*, 274(1), 142–150.
- 1019 Recanati, A., Kurz, M. D., Warren, J. M., & Curtice, J. (2012). Helium distribution in a
1020 mantle shear zone from the Josephine Peridotite. *Earth and Planetary Science Letters*,
1021 359, 162–172.
- 1022 Ruzi , L., & Moreira, M. (2010). Magma degassing process during Plinian eruptions. *Journal*
1023 *of Volcanology and Geothermal Research*, 192(3–4), 142–150.
- 1024 Sarda, P., Moreira, M., Staudacher, T., Schilling, J., & All gre, C. J. (2000). Rare gas
1025 systematics on the southernmost Mid-Atlantic Ridge: Constraints on the lower mantle
1026 and the Dupal source. *Journal of Geophysical Research: Solid Earth*, 105(B3), 5973–
1027 5996.
- 1028 Shimojuku, A., Kubo, T., Ohtani, E., Nakamura, T., Okazaki, R., Dohmen, R., &
1029 Chakraborty, S. (2009). Si and O diffusion in (Mg, Fe) 2SiO_4 wadsleyite and
1030 ringwoodite and its implications for the rheology of the mantle transition zone. *Earth*
1031 *and Planetary Science Letters*, 1(284), 103–112.
- 1032 Smye, A. J., Jackson, C. R. M., Konrad-Schmolke, M., Hesse, M. A., Parman, S. W., Shuster,
1033 D. L., & Ballentine, C. J. (2017). Noble gases recycled into the mantle through cold
1034 subduction zones. *Earth and Planetary Science Letters*, 471, 65–73.

- 1035 Staudacher, T., & Allègre, C. J. (1988). Recycling of oceanic crust and sediments: the noble
1036 gas subduction barrier. *Earth and Planetary Science Letters*, 89(2), 173–183.
- 1037 Thieme, M., Demouchy, S., Mainprice, D., Barou, F., & Cordier, P. (2018). Stress evolution
1038 and associated microstructure during transient creep of olivine at 1000–1200° C. *Physics
1039 of the Earth and Planetary Interiors*, 278, 34–46.
- 1040 Thomas, J. B., Cherniak, D. J., & Watson, E. B. (2008). Lattice diffusion and solubility of
1041 argon in forsterite, enstatite, quartz and corundum. *Chemical Geology*, 253(1–2), 1–22.
1042 <https://doi.org/10.1016/j.chemgeo.2008.03.007>
- 1043 Trieloff, M., Kunz, J., & Allègre, C. J. (2002). Noble gas systematics of the Réunion mantle
1044 plume source and the origin of primordial noble gases in Earth’s mantle. *Earth and
1045 Planetary Science Letters*, 200(3), 297–313.
- 1046 Trieloff, M., Kunz, J., Clague, D. A., Harrison, D., & Allègre, C. J. (2000). The nature of
1047 pristine noble gases in mantle plumes. *Science*, 288(5468), 1036–1038.
- 1048 Trull, T. W., & Kurz, M. D. (1993). Experimental measurements of ³He and ⁴He mobility in
1049 olivine and clinopyroxene at magmatic temperatures. *Geochimica et Cosmochimica
1050 Acta*, 57(6), 1313–1324. [https://doi.org/10.1016/0016-7037\(93\)90068-8](https://doi.org/10.1016/0016-7037(93)90068-8)
- 1051 Valbracht, P. J., Staudacher, T., Malahoff, A., & Allègre, C. J. (1997). Noble gas systematics
1052 of deep rift zone glasses from Loihi Seamount, Hawaii. *Earth and Planetary Science
1053 Letters*, 150(3), 399–411.
- 1054 Van Orman, J. A., Fei, Y., Hauri, E. H., & Wang, J. (2003). Diffusion in MgO at high
1055 pressures: Constraints on deformation mechanisms and chemical transport at the
1056 core-mantle boundary. *Geophysical Research Letters*, 30(2).
- 1057 Wang, K., Brodholt, J., & Lu, X. (2015). Helium diffusion in olivine based on first principles
1058 calculations. *Geochimica et Cosmochimica Acta*, 156, 145–153.
- 1059 Watson, E. B., Thomas, J. B., & Cherniak, D. J. (2007). ⁴⁰Ar retention in the terrestrial

1060 planets. *Nature*, 449(7160), 299.

1061 White, W. M. (1985). Sources of oceanic basalts: Radiogenic isotopic evidence. *Geology*,
1062 13(2), 115–118.

1063 Yamamoto, J., Nishimura, K., Sugimoto, T., Takemura, K., Takahata, N., & Sano, Y. (2009).
1064 Diffusive fractionation of noble gases in mantle with magma channels: origin of low
1065 He/Ar in mantle-derived rocks. *Earth and Planetary Science Letters*, 280(1), 167–174.

1066 Zhang, Y. (2014). Degassing history of Earth.

1067 Zhang, Y., & Liu, L. (2012). On diffusion in heterogeneous media. *American Journal of*
1068 *Science*, 312(9), 1028–1047.

1069 Zindler, A., & Hart, S. (1986). Chemical geodynamics. *Annual Review of Earth and*
1070 *Planetary Sciences*, 14(1), 493–571.

1071

1072

1073 *Figure captions*

1074 Fig. 1: Sample assembly for doping experiments. The assembly was annealed at 0.30 ± 0.01
1075 GPa and 1060 ± 25 °C during 24 h, using a Paterson press.

1076

1077 Fig. 2: (a) SEM image of the sample RDPC1, TEM images of microstructures in
1078 polycrystalline samples (b) RDPC1 and (c) RDPP1, and HR-TEM image of a characteristic
1079 grain boundary in (d) RDPC1.

1080

1081 Fig. 3: Arrhenius diagrams for ^{40}Ar , ^{38}Ar , and ^{36}Ar diffusion coefficients obtained from step
1082 heating analyses of polycrystalline olivine samples (a) RDPC1, (b) RDPP1, and (c) RDPP1-2.

1083

1084 Fig. 4: Isotopic diffusivity ratios (a) D_{40}/D_{36} , (b) D_{40}/D_{38} , and (c) D_{36}/D_{38} as a function of
1085 temperature. The dotted vertical line expresses the estimated boundary between the C- and
1086 supposed B-regimes of diffusion (as determined in supplementary materials). Gray lines
1087 represent the mean values of the diffusivity ratios in the C-regime, and gray areas the standard
1088 deviation about the mean. Black lines represent the values of the diffusion coefficient ratios
1089 predicted by Graham's law.

1090

1091 Fig. 5: Olivine lattice diffusion parameters for Ar from literature and retreated from Burnard
1092 et al. (2015). (a) Logarithm of the pre-exponential factors calculated for $a =$ half the grain
1093 size, and (b) activation energies. Black dashed lines represent the mean values of the
1094 corresponding diffusion parameter calculated from Futagami et al. (1993) and retreated data
1095 from Burnard et al. (2015), and gray areas give associated errors (standard deviation).

1096

1097 Fig. 6: Arrhenius diagram of grain boundary diffusion for each sample from this study
1098 calculated considering (a) $a =$ half the sample size and (b) $a =$ the grain boundary network.
1099 The corresponding diffusion parameters are reported in Table 3. The resulting mean values of
1100 grain boundary diffusivities (gray lines) are compared with lattice diffusivities (black dashed
1101 lines). Gray areas show errors on the means.

1102

1103 Fig. 7: The proportion of Ar stored at grain boundaries (black lines) and in the mineral lattice
1104 (gray lines) as a function of grain size for $s = 10^5$ (solid lines) and for $s = 10^4$ (dashed lines).
1105 The dark gray shaded areas represents the typical mantle grain size range (see Hiraga et al.,
1106 2010) and the light gray area represents the recorded grain size range of mantle peridotites
1107 (e.g., Karato, 1989; Hiraga et al., 2010).

1108

1109 Fig. 8: Durations of the boundary times t' between the B- and C-regimes and t'' between the
1110 A- and B-regimes expressed as a function of grain size for (a) $s = 10^5$ and (b) $s = 10^4$ at 600,
1111 800, 1000, and 1400 °C. The gray shaded area represents the typical mantle grain size range
1112 (Karato, 1989; Hiraga et al., 2010).

1113

1114 *Table captions*

1115 Table 1: Experimental conditions, sample descriptions, average grain sizes obtained from
1116 SEM-EBSD maps, and analytical protocols for step heating noble gas analyses, as described
1117 in Delon et al. (2018).

1118

1119 Table 2: Ar diffusion parameters (Ea and $\log(D_0/a^2)$), minimum molar segregation factors
1120 (χ_{min}), and minimum segregation factors (s_{min}) in polycrystalline olivine obtained for each
1121 sample and each isotope.

1122

1123 Table 3: Activation energies (Ea) and pre-exponential factors (D_0) obtained for each sample
1124 by considering a as half the sample size ($a = 150 \mu\text{m}$) or equivalent to the grain boundary
1125 network ($a = 0.48 \mu\text{m}$).

1126

1127

1128

1129

1130

1131

1132

1133

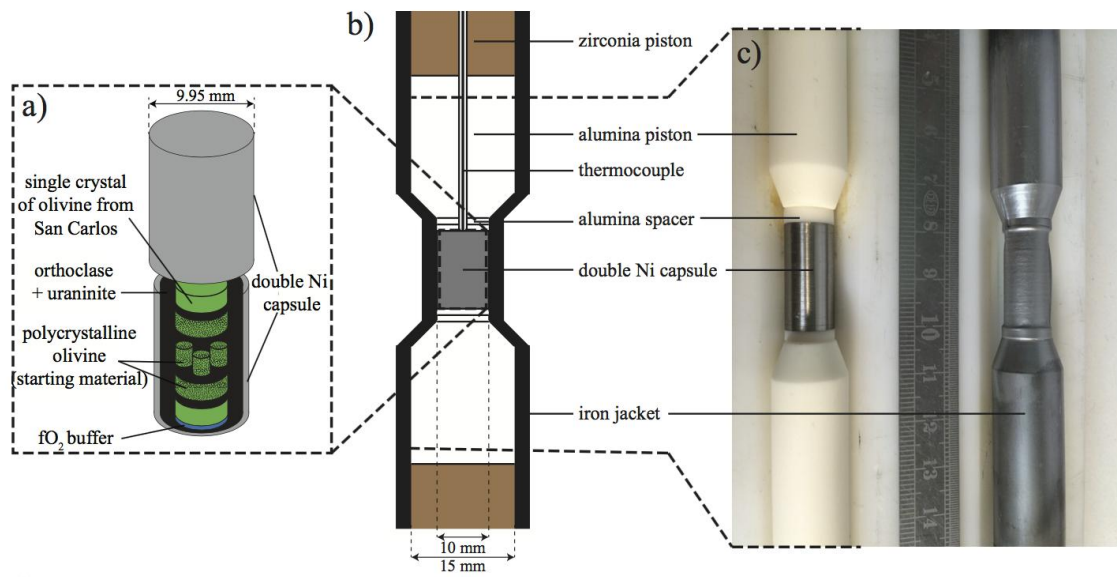


Figure 1

1134

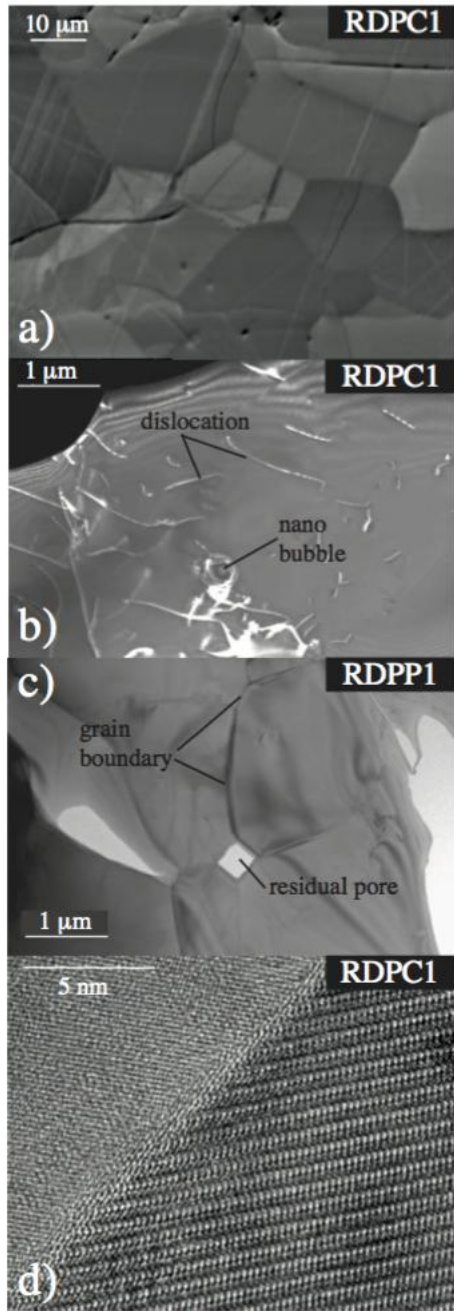
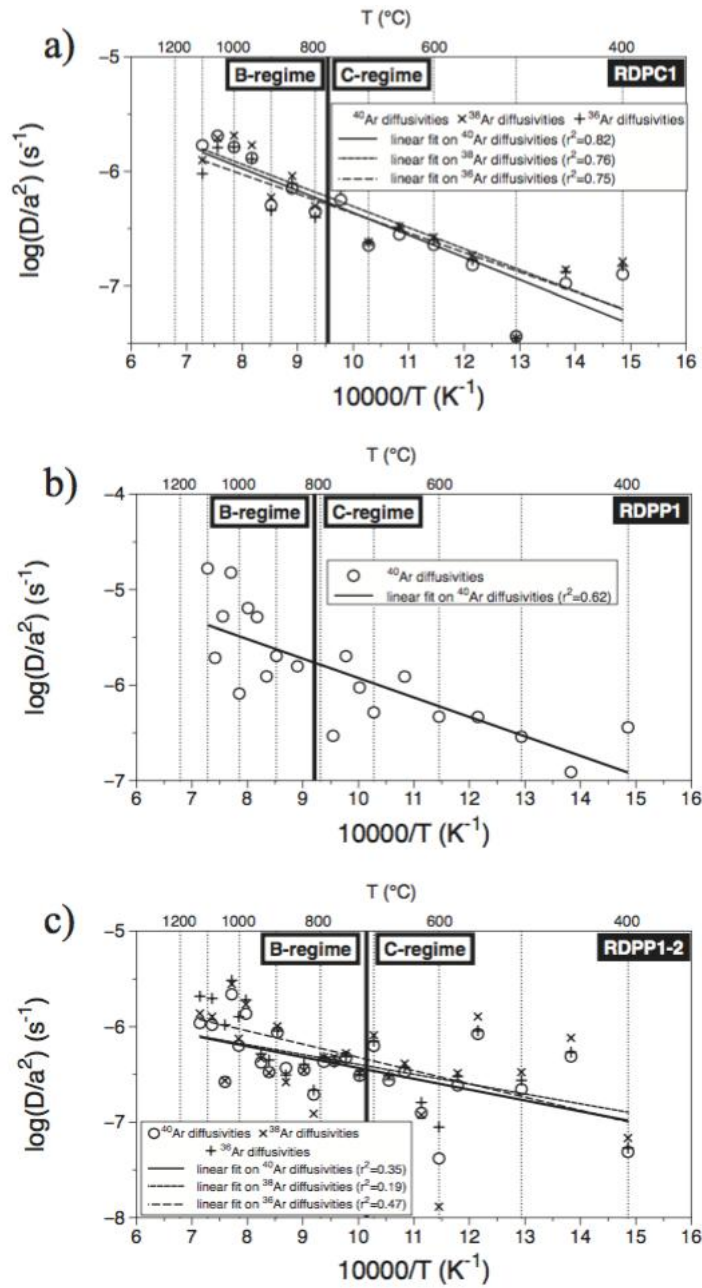


Figure 2

1135

1136



1137

1138 Figure 3

1139

1140

1141

1142

1143

1144

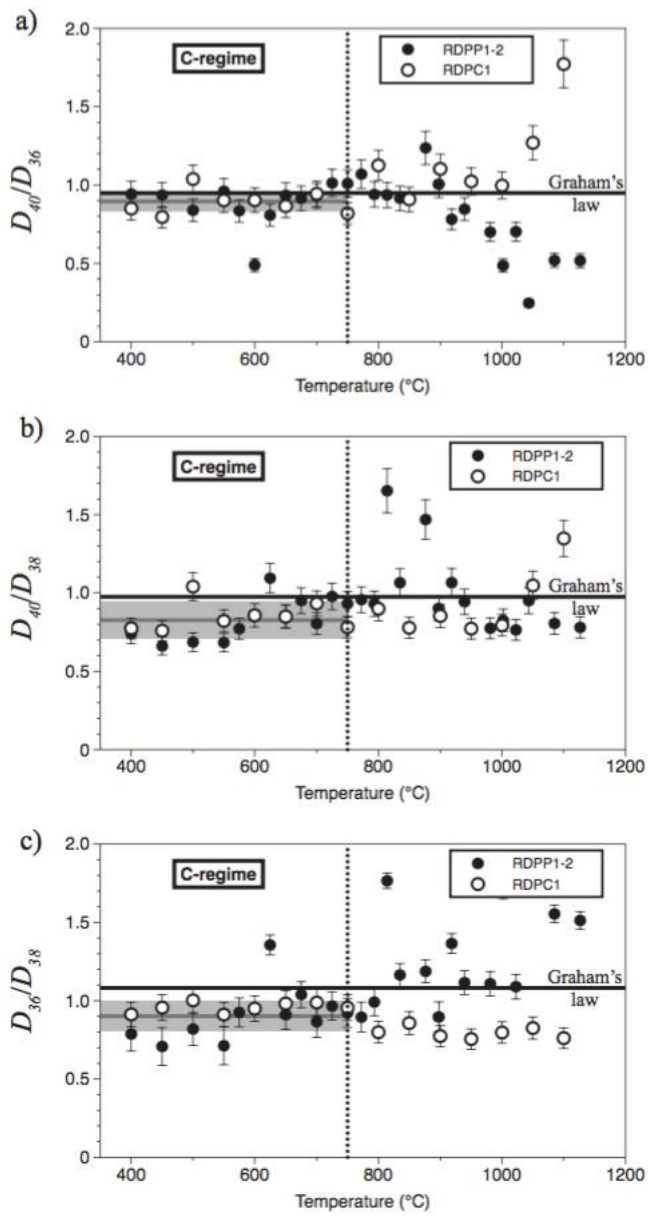


Figure 4

1145

1146

1147

1148

1149

1150

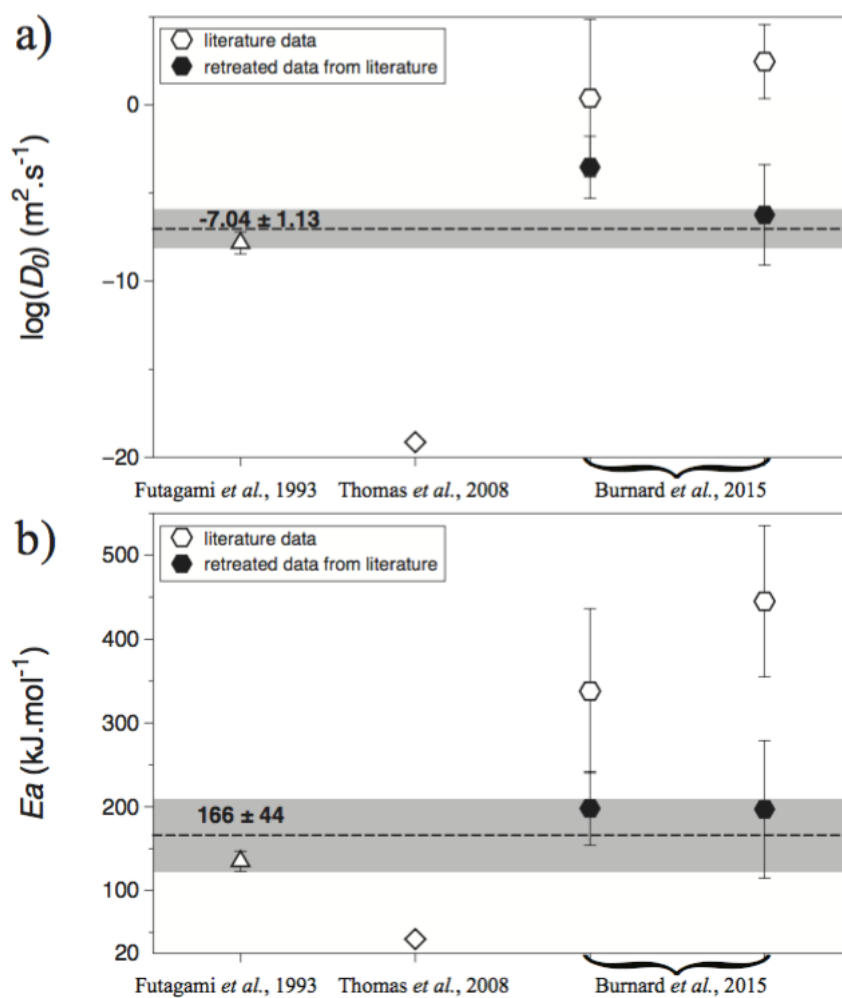


Figure 5

1151

1152

1153

1154

1155

1156

1157

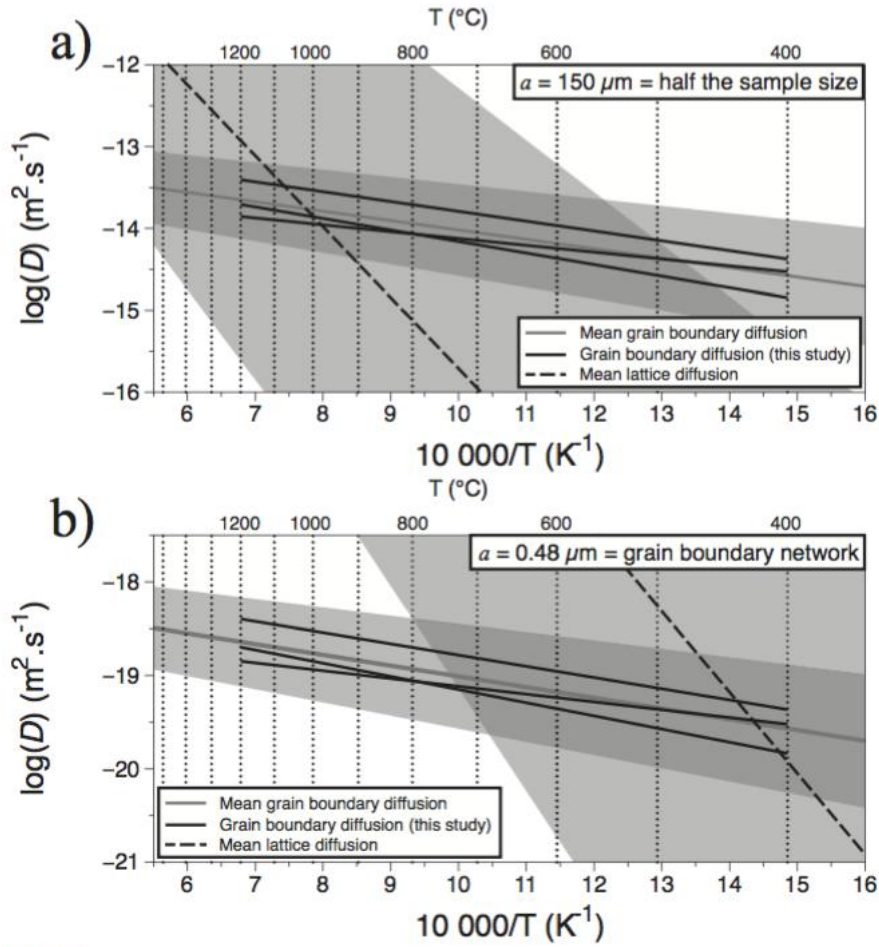


Figure 6

1158
 1159
 1160
 1161
 1162
 1163
 1164
 1165
 1166
 1167
 1168
 1169

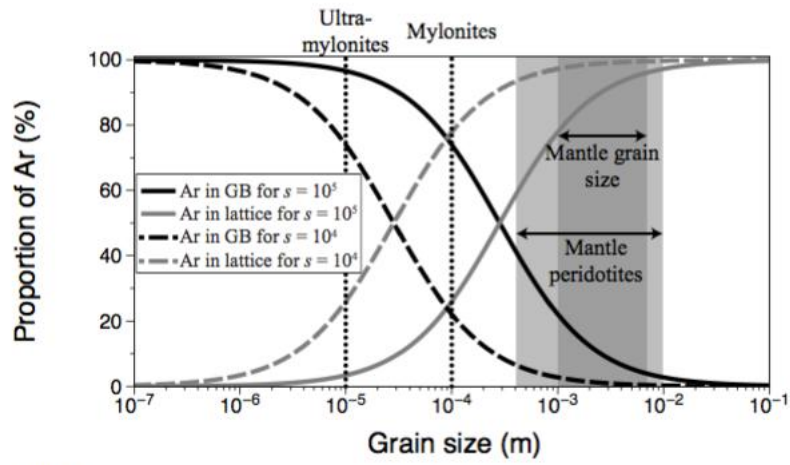


Figure 7

1170

1171

1172

1173

1174

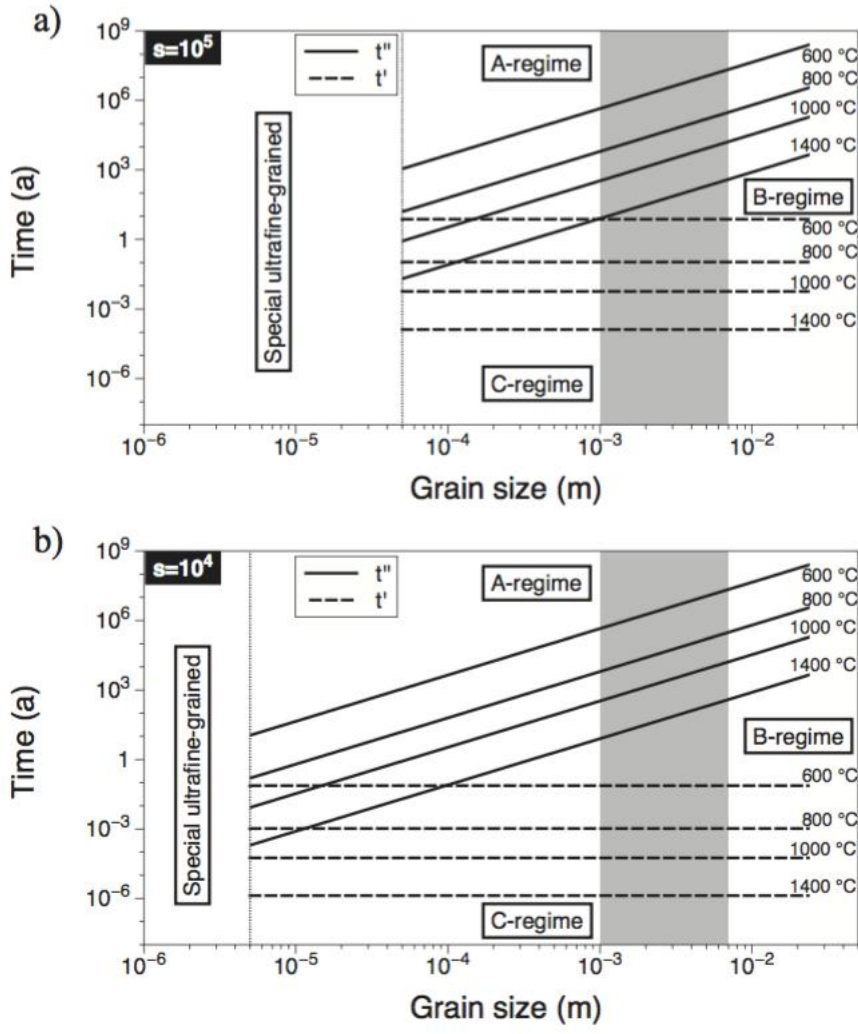


Figure 8

1175
 1176
 1177
 1178
 1179
 1180
 1181
 1182
 1183
 1184

Table 1

Type of experiment	Temperature °C	Pressure MPa	Duration	Sample	Mass mg	Grain size µm
<i>Sintering experiments</i>						
Paterson Press	1225 ± 25	305 ± 10	5 h	RDPP1	–	8.8
Piston cylinder	1275 ± 15	1000 ± 20	96 h	RDPC1	–	16.3
<i>Doping experiments</i>						
Paterson Press	1060 ± 25	305 ± 10	24 h	RDPP1	350	8.8
				RDPC1	13	16.3
				Orthoclase	353	–
<i>Step heating experiments</i>						
Helix MC Plus	Every 50 °C from 400 to 1100 °C	around 10 ⁻¹²	15 or 30 min per step	RDPC1	1.39	16.3
Helix MC Plus	Every 25 or 50 °C from 400 to 1100 °C	around 10 ⁻¹²	30 min per step	RDPP1	2.18	8.8
Helix MC Plus	Every 25 or 50 °C from 400 to 1200 °C	around 10 ⁻¹²	30 min per step	RDPP1-2	11.14	8.8

N.B. Data treatment is detailed in the main text and is identical to the procedure detailed in Delon et al. (2018).

Table 2

Sample	Ar isotope	Ea in the LAT+GB temperature range $\text{kJ}\cdot\text{mol}^{-1}$	$\text{Log}(D_0/a^2)$ in the LAT+GB temperature range s^{-1}	Minimum molar segregation factor χ_{min}	Minimum segregation factor s_{min}
RDPC1	^{40}Ar	37 ± 10	-4.42 ± 0.54	0.67 ± 0.05	3830 ± 306
	^{38}Ar	35 ± 12	-4.46 ± 0.62	0.71 ± 0.06	4097 ± 328
	^{36}Ar	33 ± 12	-4.66 ± 0.60	0.62 ± 0.05	3566 ± 285
RDPP1	^{40}Ar	39 ± 14	-3.89 ± 0.78	3.67 ± 0.29	11372 ± 910
RDPP1-2	^{40}Ar	22 ± 10	-5.27 ± 0.62	0.87 ± 0.07	2687 ± 215
	^{38}Ar	20 ± 16	-5.36 ± 0.88	1.00 ± 0.08	3097 ± 248
	^{36}Ar	27 ± 12	-4.93 ± 0.60	1.14 ± 0.09	3544 ± 284

N.B. For dimension consistency, activation energies are calculated with $a = 1$ m, since activation energies do not depend on the value of a (see Burnard et al., 2015 for discussion)

Table 3

Sample	Ea (kJ·mol ⁻¹)	$\log(D_0/a^2)$	$\log(D_0)$ $a = 0.48 \mu\text{m}^*$	$\log(D_0)$ $a = 150 \mu\text{m}^{**}$
RDPC1	27 ± 12	-5.1 ± 0.8	-17.7 ± 0.8	-12.8 ± 0.8
RDPP1	23 ± 11	-4.9 ± 0.7	-17.6 ± 0.7	-12.6 ± 0.7
RDPP1-2	16 ± 16	-5.6 ± 1.3	-18.3 ± 1.3	-13.3 ± 1.3
Mean value	22	-5.2 ± 0.3	-17.9 ± 0.3	-12.9 ± 0.3

*grain boundary network

**half the sample size